Quarterly Technical Report

Solid State Research

1986:4

Lincoln Laboratory

MASSACHUSETTS INSTITUTE OF TECHNOLOGY
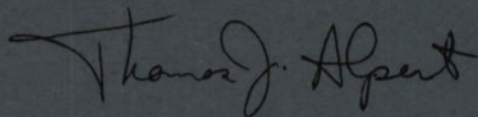
LEXINGTON, MASSACHUSETTS

The views and conclusions contained in this document are those of the contractor and should not be interpreted as necessarily representing the official policies, either expressed or implied, of the United States Government.

The ESD Public Affairs Office has reviewed this report, and it is releasable to the National Technical Information Service, where it will be available to the general public, including foreign nationals.

This technical report has been reviewed and is approved for publication.

FOR THE COMMANDER

Thomas J. Alpert, Major, USAF
Chief, ESD Lincoln Laboratory Project Office

MASSACHUSETTS INSTITUTE OF TECHNOLOGY
LINCOLN LABORATORY

SOLID STATE RESEARCH

QUARTERLY TECHNICAL REPORT

1 AUGUST — 31 OCTOBER 1986

ISSUED 19 MARCH 1987

Approved for public release; distribution unlimited.

LEXINGTON   MASSACHUSETTS

ABSTRACT

This report covers in detail the solid state research work of the Solid State Division at Lincoln Laboratory for the period 1 August through 31 October 1986. The topics covered are Solid State Device Research, Quantum Electronics, Materials Research, Microelectronics, and Analog Device Technology. Funding is provided primarily by the Air Force, with additional support provided by the Army, DARPA, Navy, SDIO, NASA, and DOE.

TABLE OF CONTENTS

LIST OF ILLUSTRATIONS

viii

ix

xi

INTRODUCTION

1. SOLID STATE DEVICE RESEARCH

Electroabsorption spectra of InGaAs/GaAs multiple quantum wells have been measured and are consistent with a type II (staggered) heterojunction band lineup for the light-hole valence band and the conduction band. This lineup arises from strain-induced splittings and shifts of the valence bands, and gives rise to a situation in which an applied electric field causes an excitonic level to be created.

A 3×1-mm monolithic two-dimensional array of 112 mass-transported lasers with integrated beam deflectors has been fabricated with good uniformity. The total CW output is thermally limited to 670 mW.

The small-signal modulation characterisitcs of GaInAsP diode lasers grown on p-type substrates have been studied on devices in which the parasitic bonding pads have been eliminated. A small-signal -3-dB frequency as high as 16.4 GHz has been measured with a 175-μm-long laser.

2. QUANTUM ELECTRONICS

A tunable, single-frequency, unidirectional, CW ring laser has been operated using Ti:Al$_2$O$_3$ as the active medium. The output power at 12,985 cm^{-1} is 20 mW for an absorbed power of 2 W from an Ar-ion laser pump.

The parasitic upconversion rate of Er:YAG has been measured and has been used along with a rate equation model to predict the effect of upconversion on the threshold and slope efficiency of an Er:YAG laser. The predictions are shown to agree with previous Er:YAG laser experiments.

Sodium resonance radiation has been generated by sum-frequency mixing the output radiation of two CW Nd:YAG lasers each of which included an intracavity etalon for wavelength tuning. When tuned to the sodium D$_2$ transition, the sum radiation was found to be completely absorbed in a high-density (10^{11} atoms/cm^3) sodium cell.

The band structure of AlGaAs/GaAs coupled quantum wells has been studied as a function of electric field applied normal to the plane of the wells, using luminescence-excitation spectroscopy and reflectivity. Crossings of several levels, a linear Stark shift, and an overall sensitivity of the spectra with respect to applied field are observed, which are uncharacteristic of single quantum well systems but are readily understood with a coupled quantum well model.

3. MATERIALS RESEARCH

A self-aligned process has been developed for fabricating radiation-hardened junction field-effect transistors (JFETs) in zone-melting-recrystallized Si films on SiO$_2$-coated Si substrates. This process has been used to fabricate n-JFETs that exhibit low threshold voltage shift ($<$$-75$ mV) and small transconductance degradation ($\sim$30 percent) for exposure to total-dose radiation of 10^8 rad(Si).

Operation of GaAs/AlGaAs diode lasers fabricated on (110) GaAs substrates has been achieved for the first time. The operating characteristics of these devices, which utilize double heterostructures grown by organometallic vapor-phase epitaxy, are comparable to those reported for diode lasers of similar structure on (100) substrates.

4. MICROELECTRONICS

Point-contact transistors and Schottky diodes have been formed on boron-doped diamond. Transistors with larger than unity gain were measured.

Chlorine ion-beam-assisted etching has been used to produce channels with sloping walls in GaAs and AlGaAs layers. Contours have been generated by tilting the substrate with respect to the etching beams at an angle that is either fixed or varied by means of a computer-controlled stage.

Charge amplification has been achieved in a charge-coupled device by using impact ionization in a high-field region between adjacent gates. The measured noise of this process agrees well with existing theory.

GaAs MESFETs with 0.3-μm gate length have been fabricated using masked ion-beam lithography to define self-aligned submicrometer gates, and optical lithography to define areas for contact pads and device isolation. The fabricated devices have a transconductance of 150 mS/mm.

5. ANALOG DEVICE TECHNOLOGY

Convolution of an image with an electronically controllable Gaussian kernel function has been carried out in the focal plane of a large CCD imager operating with standard television timing. Off-chip subtraction of the Gaussian-convolved images and subsequent thresholding were used to perform edge extraction in real time using the difference-of-Gaussians algorithm.

SAW/FET devices have been fabricated that exhibit 100 MHz of programmable bandwidth and a 30-dB tap on/off ratio. A peak-to-side-lobe ratio of 27 dB has been achieved in the matched filtering of 31-chip-long m-sequences, and CW interference has been adaptively suppressed by 24 dB.

As the first step in developing laser etching of thin films on surface-acoustic-wave reflective-array compressors (RACs) to adjust phase and amplitude response, the effects of spatial-impulse-like patterns etched into phase-compensating Mo and amplitude-compensating cermet films have been measured. The results compare favorably with analytical predictions based on the weak-reflection RAC model and show the expected coupling of phase and amplitude adjustments.

REPORTS ON SOLID STATE RESEARCH

1 August through 31 October 1986

PUBLISHED REPORTS

Journal Articles

JA No.

5801	Theoretical Temperature Dependence of Solar Cell Parameters	J.C.C. Fan*	Solar Cells **17**, 309 (1986)
5810	Characterization and Entrainment of Subboundaries and Defect Trails in Zone-Melting-Recrystallized Si Films	M.W. Geis H.I. Smith* C.K. Chen	J. Appl. Phys. **60**, 1152 (1986), DTIC AD-A172571
5830	Electron-Pumped High-Efficiency Semiconductor Laser	V. Daneu D.P. DeGloria A. Sanchez F. Tong* R.M. Osgood, Jr.*	Appl. Phys. Lett. **49**, 546 (1986)
5864	A Technology for Optical Interconnections Based on Multichip Integration	D.Z. Tsang D.L. Smythe A. Chu* J.J. Lambert	Opt. Eng. **25**, 1127 (1986)
5865	Monolithic Integration of GaAs/AlGaAs Double-Heterostructure LED's and Si MOSFET's	H.K. Choi G.W. Turner T.H. Windhorn B-Y. Tsaur	IEEE Electron Device Lett. **EDL-7**, 500 (1986)
5890	SAW-Based 100 MHz-Bandwidth Adaptive Filter	D.E. Oates J.B. Green P.M. Grant	Electron Lett. **22**, 998 (1986)

---

* Author not at Lincoln Laboratory.

Meeting Speeches

MS No.

6935	AlGaAs Optoelectronic Devices on Monolithic GaAs/Si Substrates	T.H. Windhorn G.M. Metze	In *Optical Fiber Sources and Detectors*, Proc. SPIE **587**, 158-163 (1985)
6935A	GaAs/AlGaAs Diode Lasers on Monolithic GaAs/Si Substrates	T.H. Windhorn G.W. Turner G.M. Metze	Materials Research Society Symposium Proc., Vol. 67, Palo Alto, California, 15-18 April 1986, p. 157
6995	Diode-Laser Infrared Hetero-dyne Radiometer at 28 μm	D.L. Spears R.E. Reeder	*Conference Record, Tenth International Conference on Infrared and Millimeter Waves*, R.J. Temkin, Ed. (IEEE, New York, 1985), pp. 75-76
7015	Capping Techniques for Zone-Melting-Recrystallized Si-on-Insulator Films	C.K. Chen L. Pfeiffer* K.W. West* M.W. Geis S. Darack* G. Achaibar* R.W. Mountain B-Y. Tsaur	Materials Research Society Symposium Proc., Vol. 53, Boston, 2-6 December 1985, pp. 53-58
7019	Assessment of Silicon-on-Insulator Technologies for VLSI	B-Y. Tsaur	Materials Research Society Symposium Proc., Vol. 53, Boston, 2-6 December 1985, pp. 365-373
7047A	Monolithic Integration of Si and GaAs Devices	H.K. Choi G.W. Turner B-Y. Tsaur T.H. Windhorn	Materials Research Society Symposium Proc., Vol. 67, Palo Alto, California, 15-18 April 1986, pp. 165-171

---

* Author not at Lincoln Laboratory.

---

* Author not at Lincoln Laboratory.

UNPUBLISHED REPORTS

Journal Articles

JA No.

5859	Observation of Gain Compression in a GaAlAs Diode Laser Through a Picosecond Transmission Measurement	B.C. Johnson A. Mooradian	Accepted by Appl. Phys. Lett.
5872	Laser Remote Sensing of the Atmosphere	D.K. Killinger N. Menyuk	Accepted by Science
5878	Large Room Temperature Effects from Resonant Tunneling Through AlAs Barriers	W.D. Goodhue T.C.L.G. Sollner H.Q. Le E.R. Brown B.A. Vojak	Accepted by Appl. Phys. Lett.
5880	Prevention of Current Leakage in Mass-Transported GaInAsP/InP Buried-Heterostructure Lasers with Narrow Transported Regions	Z.L. Liau J.N. Walpole	Accepted by IEEE J. Quantum Electron.
5891	Attainment of 0.13-μm Lines and Spaces by Excimer-Laser Projection Lithography in Diamond-Like Carbon Resist	M. Rothschild D.J. Ehrlich	Accepted by Am. Vac. Soc.
5892	Laser-Direct-Writing Process: Metal Deposition, Etching, and Applications to Microcircuits	J.G. Black D.J. Ehrlich M. Rothschild S.P. Doran J.H.C. Sedlacek	Accepted by J. Vac. Sci. Technol.
5896	Laser Photochemical Etching of Molybdenum and Tungsten Thin Films by Surface Halogenation	M. Rothschild J.H.C. Sedlacek D.J. Ehrlich	Accepted by Appl. Phys. Lett.
5900	Visible-Laser Photochemical Etching of Cr, Mo, and W	M. Rothschild J.H.C. Sedlacek J.G. Black D.J. Ehrlich	Accepted by J. Vac. Sci. Technol.

---

* Titles of Meeting Speeches are listed for information only. No copies are available for distribution.

MS No.

7207	Monolithic Integration of Si and GaAs Devices	H.K. Choi G.W. Turner T.H. Windhorn B-Y. Tsaur	SPIE Fiber/LASE '86, Cambridge, Massachusetts, 14-26 September 1986
7223	On-Wafer Testing of GaInAsP/InP Mass-Transported Lasers	J.N. Walpole Z.L. Liau	
7049A	Growth and Characterization of Ti:Al$_2$O$_3$ Crystals for Laser Applications	A.J. Strauss R.E. Fahey A. Sanchez R.L. Aggarwal	30th Annual International Symposium on Optical and Optoelectronic Engineering, San Diego, California, 17-22 August 1986
7071B	Resonant-Tunneling and Coupled Well Devices	T.C.L.G. Sollner W.D. Goodhue C.A. Correa	Laser Seminar, Univ. of Rochester, Rochester, New York, 25 September 1986
7095A	Artificial Neural Network Implementations Using Charge-Coupled Device and MNOS Nonvolatile Analog Memory Technologies	J.P. Sage	NSF Workshop on Neural Networks and Neuromorphic Systems, Woburn, Massachusetts, 8 October 1986
7135B	Picosecond Characterization of the Permeable Base Transistor	D.R. Dykaar* G.A. Mourou* M.A. Hollis B.J. Clifton K.B. Nichols C.O. Bozler R.A. Murphy	1986 GaAs Integrated Circuit Symposium, Grenelefe, Florida, 28-30 October 1986
7162A	Laser Direct Patterning of Submicrometer Structures	D.J. Ehrlich	American Vacuum Society Silicon Processing Symposium, Buena Vista, Florida, 7 October 1986

---

* Author not at Lincoln Laboratory.

---

* Author not at Lincoln Laboratory.

---

* Author not at Lincoln Laboratory.

ORGANIZATION

SOLID STATE DIVISION

A.L. McWhorter, *Head*
I. Melngailis, *Associate Head*
E. Stern, *Associate Head*
J.F. Goodwin, *Assistant*

N.L. DeMeo, Jr., *Associate Staff*

QUANTUM ELECTRONICS

A. Mooradian, *Leader*
P.L. Kelley, *Associate Leader*

Aggarwal, R.L.
Barch, W.E.
Belanger, L.J.
Brailove, A.A.
Daneu, V.
DeFeo, W.E.
Feldman, B.
Hancock, R.C.
Harrison, J.*
Jeys, T.H.
Killinger, D.K.
Le, H.Q.

Menyuk, N.
Sanchez-Rubio, A.
Seppala, J.P.
Schulz, P.A.
Sharpe, K.A.
Sullivan, D.J.
Tong, F.F-K.*
Wall, K.F.
Walker, W.P.
Walther, A.
Zayhowski, J.J.

ELECTRONIC MATERIALS

A.J. Strauss, *Leader*
B-Y. Tsaur, *Assistant Leader*
H.J. Zeiger, *Senior Staff*

Anderson, C.H., Jr.
Button, M.J.
Chen, C.K.
Choi, H.K.
Connors, M.K.
Delaney, E.J.
Eglash, S.J.
Fahey, R.E.
Finn, M.C.
Iseler, G.W.

Kolesar, D.F.
Krohn, L., Jr.
Mastromattei, E.L.
Mattia, J.P.
Nitishin, P.M.
Pantano, J.V.
Tracy, D.M.
Turner, G.W.
Wang, C.A.
Windhorn, T.H.

APPLIED PHYSICS

R.C. Williamson, *Leader*
D.L. Spears, *Assistant Leader*
T.C. Harman, *Senior Staff*
R.H. Rediker, *Senior Staff*

Aull, B.F.
Betts, G.E.
Bossi, D.E.*
Chan, S.K.*
Corcoran, C.J.*
Cox, C.H., III
Diadiuk, V.
Donnelly, J.P.
Ferrante, G.A.

Groves, S.H.
Hovey, D.L.
Johnson, L.M.
Liau, Z.L.
Lind, T.A.
Metze, G.M.
Molter, L.A.*
O'Donnell, F.J.
Palmacci, S.T.

Palmateer, S.C.
Plonko, M.C.
Reeder, R.E.
Tsang, D.Z.
Walpole, J.N.
Woodhouse, J.D.
Yap, D.*
Yee, A.C.

---

* Research Assistant

ANALOG DEVICE TECHNOLOGY

R.W. Ralston, *Leader*
R.S. Withers, *Associate Leader*

Anderson, A.C.
Arsenault, D.R.
Boisvert, R.R.
Brogan, W.T.
Denneno, A.P.
DiIorio, M.S.
Dolat, V.S.
Fischer, J.H.

Fitch, G.L.
Frickey, J.M.
Green, J.B.
Holtham, J.H.
Koulman, W.A.
Lattes, A.L.
Lichtenwalner, D.J.*

Macedo, E.M., Jr.
Munroe, S.C.
Oates, D.E.
Sage, J.P.
Slattery, R.L.
Thompson, K.E.†
Wong, S.C.*

MICROELECTRONICS

W.T. Lindley, *Leader*
R.A. Murphy, *Associate Leader*
D.J. Ehrlich, *Assistant Leader*
B.B. Kosicki, *Assistant Leader*

Astolfi, D.K.
Bales, J.W.*
Bennett, P.C.
Black, J.G.
Bozler, C.O.
Brown, E.R.
Burke, B.E.
Calawa, A.R.
Chen, C.L.
Chiang, A.M.
Clifton, B.J.
Cullen, P.A.*
Daniels, P.J.
Doherty, C.L., Jr.
Doran, S.P.
Durant, G.L.
Efremow, N.N., Jr.
Felton, B.J., Jr.

Gajar, S.A.*
Geis, M.W.
Goodhue, W.D.
Gray, R.V.
Hollis, M.A.
Huang, J.C.M.
Johnson, K.F.
LeCoz, Y.L.*
Lincoln, G.A., Jr.
Lyszczarz, T.M.
Mahoney, L.J.
Maki, P.A.
Manfra, M.J.
Mathews, R.H.
McGonagle, W.H.
McIntosh, K.A.
Melngailis, J.‡

Mountain, R.W.
Nichols, K.B.
Pang, S.W.
Parker, C.D.
Pichler, H.H.
Rabe, S.
Rathman, D.D.
Reinold, J.H., Jr.
Rothschild, M.
Sedlacek, J.H.C.
Smith, F.W.*
Smythe, D.L., Jr.
Sollner, T.C.L.G.
Uttaro, R.S.
Vera, A.
Wilde, R.E.
Young, E.M.

1. SOLID STATE DEVICE RESEARCH

1.1 A NOVEL ELECTROABSORPTION EFFECT IN InGaAs/GaAs STRAINED-LAYER MULTIPLE-QUANTUM-WELL STRUCTURES

Van Eck et al.[1] recently reported band-edge absorption spectra in a 10-period $In_{0.13}Ga_{0.87}As$/GaAs multiple-quantum-well (MQW) structure with various electric fields applied perpendicular to the layers. InGaAs/GaAs is not a lattice-matched system and the influence of the layer strain on the electroabsorption spectra cannot be neglected. In particular, Marzin et al.[2] suggested that the conduction band and light-hole valence band display a type II (staggered) heterojunction band lineup due to strain-induced band shifts. We report electroabsorption of a 60-period $In_{0.2}Ga_{0.8}As$/GaAs MQW structure. This system displays a novel effect, the creation of an exciton by the applied field, which is consistent with the Marzin hypothesis.

Using molecular beam epitaxy, we fabricated a structure consisting, in order of growth, of a thick p^+-GaAs layer, an undoped 60-period $In_{0.2}Ga_{0.8}As$/GaAs MQW structure, and a thick n-GaAs layer. Thus, the MQW structure formed the intrinsic region of an n-i-p^+ structure. The layers in the MQW were 100 Å thick, as determined by transmission electron microscopy. The alloy composition was checked by secondary ion mass spectrometry.

Figure 1-1 shows absorption spectra of the sample for several voltages applied to the n-i-p^+ structure. In the zero-volt spectrum of Figure 1-1, and also in the spectra of Van Eck et al.,[1] there is one peak at the edge of each subband at 968 nm and 932 nm. These heavy-hole exciton peaks shift to lower energy, weaken, and broaden with increasing electric field. This is the usual
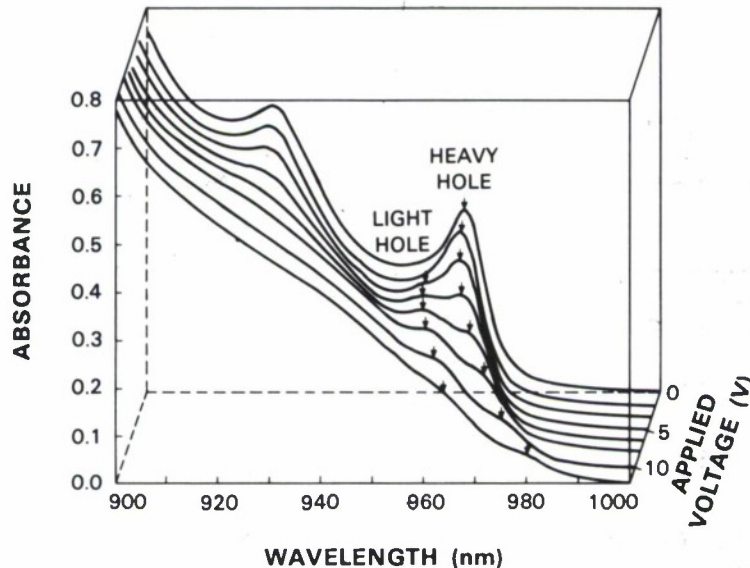
Figure 1-1. Absorbance spectra of the InGaAs/GaAs MQW for applied voltages of 0, 2, 3.5, 5, 6.5, 8, 10, and 12 V.

1

behavior seen in quantum wells and is due to the pulling apart of the exciton by the electric field. In reported electroabsorption spectra of GaAs/AlGaAs MQWs, however, two peaks are seen at the edge of the first subband, due to both heavy-hole and light-hole excitons. In the spectra of Figure 1-1, a second peak at the edge of the first subband begins to appear at 957 nm when 3.5 V is applied to the structure. As the applied voltage is increased, this peak at first grows more prominent, and then, at higher applied voltages, it shifts to lower energy, broadens and weakens. Extrapolation of the position of this peak to zero applied volts shows that it would be clearly resolvable from the main peak if it were present with the same amplitude observed at higher voltages. However, it is also too close to the main peak to be associated with a 'forbidden' transition involving an excited electron or hole subband. Therefore, it is ascribed to an exciton associated with the n = 1 electron and light-hole subbands.

The observed voltage dependence can be explained on the basis of the strain-induced splitting of the valence bands. Growth of an InGaAs/GaAs MQW structure on a GaAs substrate without internally generated misfit dislocations requires in-plane biaxial compression of the InGaAs layers. If the MQW structure is relaxed with respect to the substrate, there also will be inplane biaxial tension of the GaAs layers. In each case, the valence bands split into two anisotropic bands. In addition, the bandgap of GaAs is decreased, and the bandgap of InGaAs is increased by the strain. These effects are illustrated in Figure 1-2(a). We calculated the relative bulk band-edge energies in the two layers by the procedure of Asai and Oe,[3] using tabulated elastic constants, deformation potentials,[4] and band offsets.[5] We obtain a general result that the light-hole band edge in the InGaAs layer is lower in energy than the light-hole band edge in the
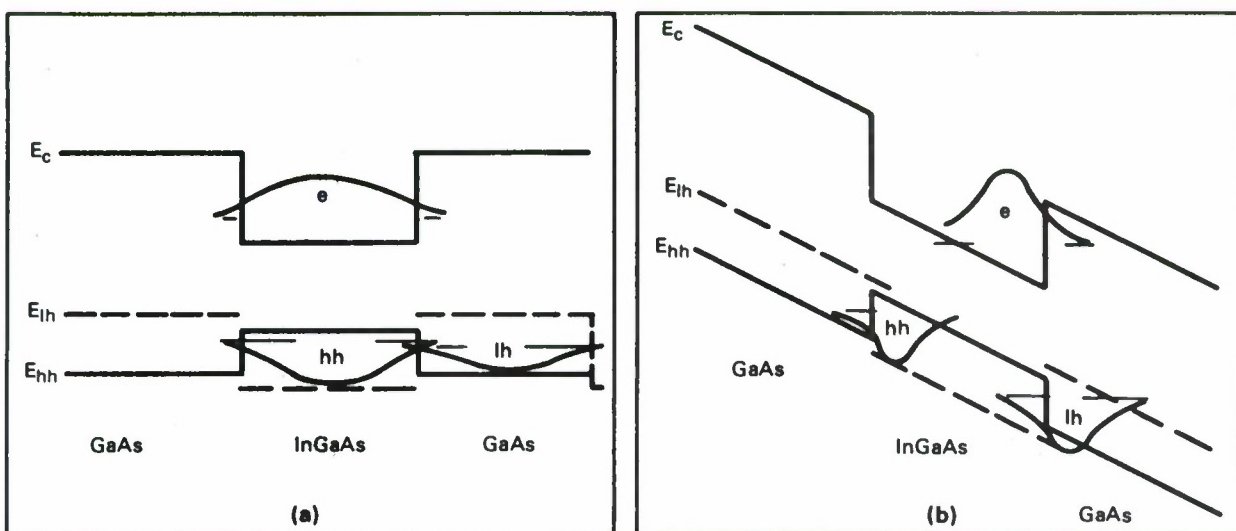
Figure 1-2. (a) Strain-induced band lineups for a free-standing InGaAs/GaAs superlattice. (b) Effect of applied electric field on the electron, heavy-hole, and light-hole wave functions.

2

GaAs layer. This result applies to an arbitrary value of In composition, and holds over the range of reported[6,7] strain-free valence band offsets. It also holds for both a 'free-standing' MQW and one that is strained to match the in-plane lattice constant of the GaAs substrate. Normally, then, the electron is mostly in the InGaAs layer and the light hole is mostly in the GaAs layer, and the two do not form an exciton because of their spatial separation. The application of an electric field causes them to be localized at the same interface as illustrated in Figure 1-2(b), and, at some critical field value, an excitonic state will form provided the light-hole well is still deep enough to confine the hole. ('Deep enough' means that the time required for the light hole to tunnel out of the well is longer than h/E_b, where E_b is the exciton binding energy. The absence of the second peak at the edge of the second subband in Figure 1-1 suggests that this criterion is not satisfied for the n = 2 light hole.)

In summary, the electroabsorption spectra of InGaAs/GaAs MQWs are consistent with a type II heterojunction band lineup for the light-hole valence band and the conduction band. In this system, the application of an electric field causes the light-hole excitonic level to form. Other reported optical measurements have suggested this type II band lineup.[2,6,7]

B.F. Aull   B.E. Burke
W.D. Goodhue   K.B. Nichols

1.2 LARGE MONOLITHIC TWO-DIMENSIONAL ARRAYS OF GaInAsP/InP SURFACE-EMITTING LASERS

We report the fabrication of a large monolithic two-dimensional array of GaInAsP/InP surface-emitting lasers, which has an overall size of 3 × 1 mm and contains a total of 112 lasers with good uniformity and high output powers. This work represents perhaps the first demonstration of a large-scale monolithic integration of diode lasers. Moreover, the monolithic 2D arrays have a number of potential applications, including very high output power, high energy-conversion efficiency and good output beam quality (when phase-locked).

The present arrays consist of buried-heterostructure lasers with integrated beam deflectors[8,9] and are fabricated by using selective chemical etching and mass transport of LPE-grown p-substrate double-heterostructure wafers. The fabrication procedures are similar to those used in the previously reported 4 × 4 arrays,[8] but the present arrays employ lasers with emissions from both ends, a higher device packing density, a larger array area and a simplified electrical connection scheme. As shown in Figure 1-3, each wafer typically contains three arrays. In each array, the lasers are arranged in a 4 × N configuration, with N being limited by the size and quality of the wafer. The four lasers in each line have a center-to-center spacing of about 250 μm and are electrically connected by a single Au pad. Each laser has a resonator cavity length of 230 μm and has two integrated beam deflectors (one at each end). The lateral spacing between adjacent lines of lasers is about 100 μm.

Each finished wafer is probed one line (four lasers) at a time, before the arrays are cut out and mounted on copper heat sinks. The probing is carried out under room-temperature CW
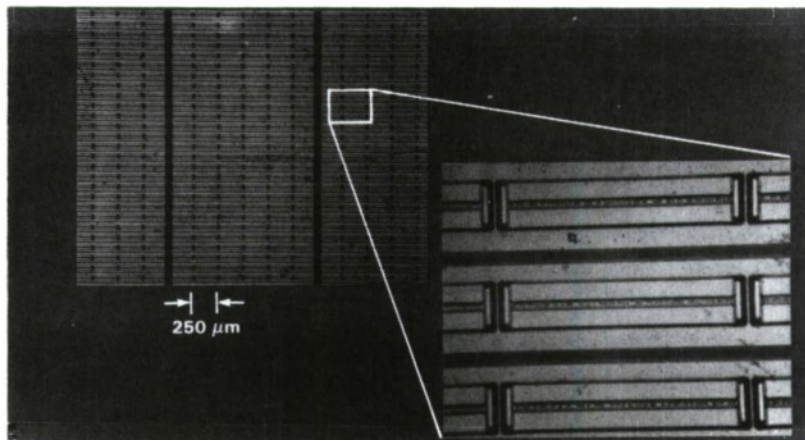
Figure 1-3. Optical photographs of a top view of the central part of a finished wafer that contains three 4 × N laser arrays. (There appear to be six lasers in each line, but the outer two are actually dummies that serve only as wire-bonding pads.) The enlarged picture shows the details of the laser mesas, the integrated beam deflectors and the Au pads. Note that there are two beam deflectors for each laser (one at each end).

conditions at a current less than 250 mA, from which preliminary data on threshold and efficiency are obtained. After probing, the defective devices are identified and only regions of uniform threshold and efficiency are selected for mounting and wire-bonding. To simplify the task of electrical connections, one single connection is used for each block of four-to-six lines of lasers. (All 16-24 lasers within each block, therefore, are electrically connected in parallel.)

Figure 1-4 shows an infrared photograph of an array operated below threshold. This array has overall dimensions of 3×1 mm and contains 116 devices. As indicated above the photograph, the array has been divided into six blocks with the exception of four devices in the middle, which have been damaged by a tweezer scratch during fabrication. The average CW threshold currents in Blocks 1, 2, 3, 4, 5 and 6 (numbered from left to right) are 24.0, 22.7, 22.4, 18.6, 19.1 and 20.2 mA per laser, respectively. When operated separately, each block shows 160 mW output power at a current of approximately 880 mA (Blocks 2, 3, and 4) or 1070 mA (Blocks 1, 5, and 6).

Figure 1-5 shows the output powers when more and more blocks of lasers are operated simultaneously. It can be seen that an output power of 230 mW is obtained from a single block of 16 lasers (Block 2). This corresponds to an average power output of 14 mW per laser and an average optical flux of 57 W/cm^2. However, when more adjacent blocks are operated simultaneously, the total power is considerably less than the sum of individually operated blocks. With all six blocks connected in parallel, a CW output of 670 mW is obtained at a total current of 6 A. These results indicate heating in the copper block on which the array is mounted. Improvement can be made with an effective heat extraction from the copper block immediately underneath the array or with further optimization of laser threshold and efficiency.

→| |← 100 μm

77713-4
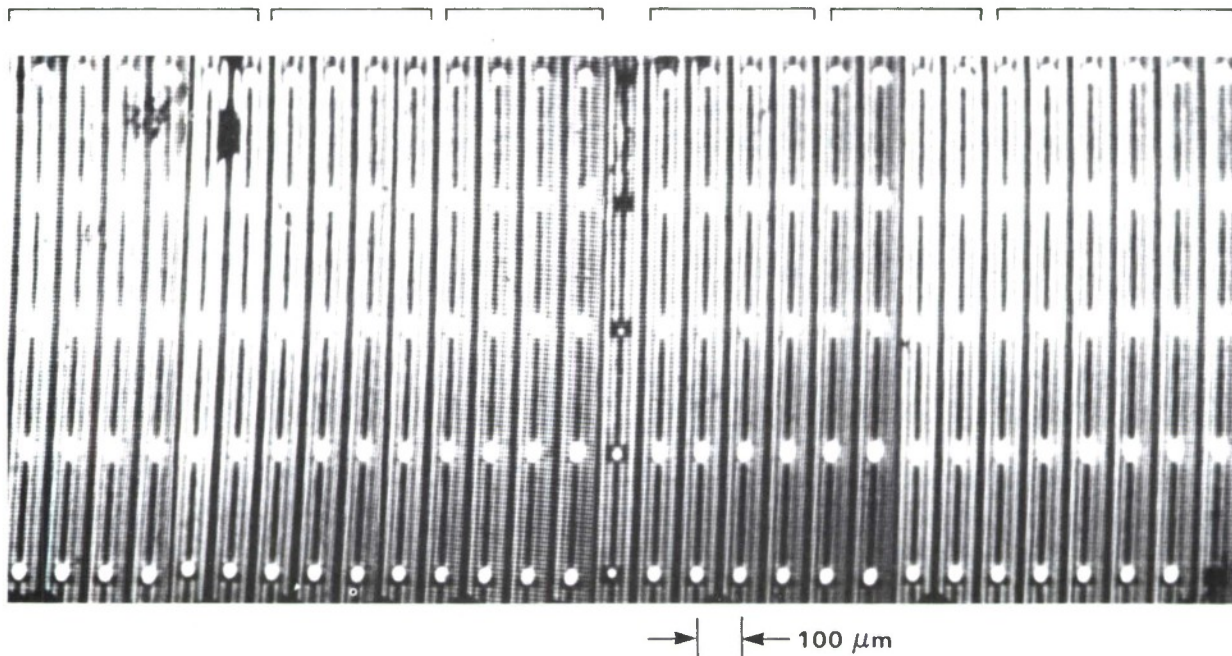
Figure 1-4. Infrared photograph of a large 2D laser array operated below threshold. This array is taken from the middle part of the wafer shown in Figure 1-3, but turned 90°. The outer rows of the light spots appear dimmer than the inside rows because the spots of light on the inside are actually two spots but unresolved. The horizontal line segments above the photograph indicate the six blocks into which the array is divided for electrical connections.
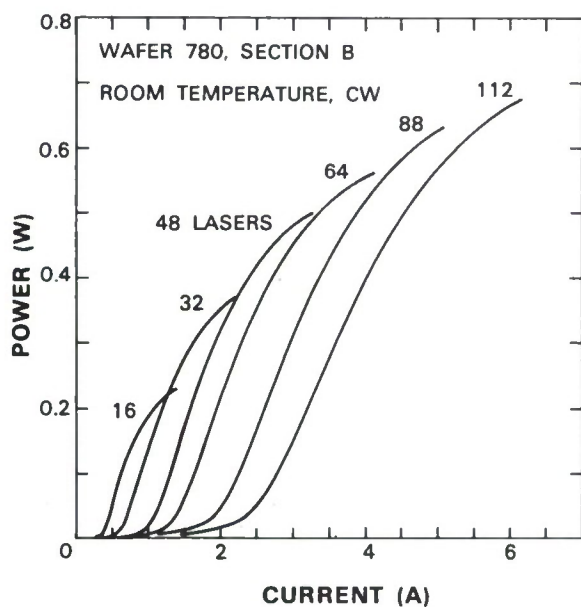
Figure 1-5. Light outputs of the monolithic laser array shown in Figure 1-4 when different numbers of lasers are operated simultaneously (and electrically connected in parallel). The six light output vs current characteristics shown are those of Blocks, 2, 3-4, 2-4, 2-5, 1-5, and 1-6, respectively. (The blocks are numbered from left to right in Figure 1-4.)

77713-5

5

In conclusion, a large-area monolithic 2D array of more than one hundred surface-emitting lasers with good uniformity has been demonstrated. The present results show a significant improvement in overall power compared to previous small arrays, although the potential for very high CW output has not been fully realized because of thermal limitations. Work is in progress to increase the efficiency of the surface-emitting lasers, to improve the heat extraction, and to phase-lock the elements of the laser arrays.

<div align="right">
Z.L. Liau

J.N. Walpole
</div>

1.3 SMALL-SIGNAL MODULATION OF p-SUBSTRATE MASS-TRANSPORTED GaInAsP/InP LASERS

The small-signal modulation characteristics of GaInAsP/InP diode lasers are of interest for the transmission of microwave signals over optical fibers. Small-signal modulation experiments have been reported for mass-transported buried-heterostructure (BH) lasers[10,11] and for similar structures based on the mass-transported laser and referred to as either vapor-phase-regrown[12] lasers or constricted-mesa vapor-phase-transported[13] lasers. This class of lasers has the highest-frequency modulation response of the various laser structures reported to date, but studies have been limited to lasers with n-type substrates. We report here the first studies of the small-signal modulation characteristics of mass-transported lasers with p-type substrates.

In the p-substrate laser,[8] the bulk of the series resistance is in the low-mobility substrate, and so the heat distribution is different from that of the n-substrate laser. Thus mounting the p-substrate laser stripe side up to minimize parasitic capacitance is also advantageous in terms of heat dissipation. The substrate type also may influence the modulation capability of the laser if the amount of zinc incorporated into the active region during the growth of the quaternary layer on the p-type substrate is different from the zinc doping in comparable n-type substrate lasers, based on work by Su et al.[12,14]

The structure of the mass-transported BH laser is shown in Figure 1-6. The laser wafer was grown by liquid phase epitaxy using a 1×10^{18} cm^{-3} Zn-doped substrate and growing a 9×10^{17} cm^{-3} Zn-doped buffer layer, a 0.2-μm-thick undoped GaInAsP active layer, and a 2×10^{18} cm^{-3} Sn-doped InP cap layer. A quaternary cap layer is not required since the small-area contact to the laser mesa is n-type. The p-type contact, which is more difficult to make with low resistance than the n-type contact, is spread over a large area in this structure, thus yielding low series contact resistance. The lasers are fabricated in a fashion similar to that described previously[10] for lasers on n-type InP substrates.

The nominal width of the GaInAsP active region is 1.5 μm and the width of the adjacent mass-transported InP regions is about 0.2 μm. After the BH structure was fabricated, the laser wafer was lapped to a thickness of 75 μm and ohmic contacts applied to the n-type and p-type regions using Au-Sn and Au-Zn, respectively. The contact metallization pads are confined to the top of the mesa, as shown in Figure 1-6, so as to minimize parasitic capacitance between the

<div align="center">6</div>

CONTACT PAD

n InP 2×10^{18}

OXIDE

GaInAsP

p InP 9×10^{17}

p InP 1×10^{18} cm^{-3}
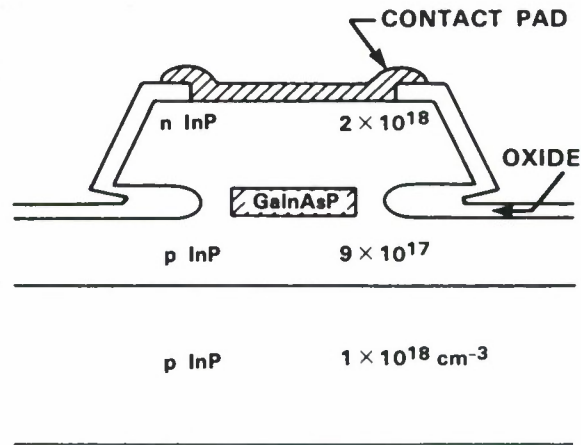
Figure 1-6.   Cross section of p-substrate mass-transported laser. Contact pad is confined to the top of the laser mesa to minimize parasitic capacitance.

contact pad and the substrate. Each laser was soldered onto a gold-plated copper heat sink with the substrate side down. Indium-coated gold ribbons connect the laser to an adjacent microstripline.

Room-temperature CW threshold currents were as small as 4.5 mA, which is the lowest threshold reported for 1.3-μm lasers. The highest optical power output was 15 mW/facet for a 175-μm device, while the best external differential quantum efficiency was 34% per facet just above threshold. Typically, thresholds of 6-15 mA and efficiencies of 18-30% were observed.

Frequency response measurements were made using a network analyzer with a reflection-transmission test set. The laser was connected to the output of the test set and an InGaAs PIN photodiode,[15] with a 3-dB roll-off frequency of about 22 GHz, was connected to the input. The light from the laser was collimated by a multi-element 40X 0.5-NA microscope objective and focused onto the detector by an identical objective. The collection optics were antireflection coated for visible light, and, as a result, only about 50% of the 1.3-μm energy was collected and sent to the focusing objective. The external quantum efficiency of the photodiode with matching resistors is about 27%.[15] The frequency dependence of the insertion loss in the laser-photodiode optical link for one of the faster lasers is shown in Figure 1-7. At a bias current of 40 mA, the low-frequency insertion loss of 36 dB contains near equal contributions due to inefficiencies in the laser, the optics, and the detector. The insertion loss is a function of laser bias current and deteriorates by 5 dB at low frequencies when the laser is operated at a current of 90 mA or 15 times the 6-mA threshold. This deterioration of the insertion loss is probably due to the drop in the differential quantum efficiency at high bias currents. At 90 mA, the 3-dB roll-off frequency of the laser is 16.4 GHz. The highest 3-dB roll-off frequencies of three 175-μm-long lasers varied from 12.6 to 16.4 GHz.

7
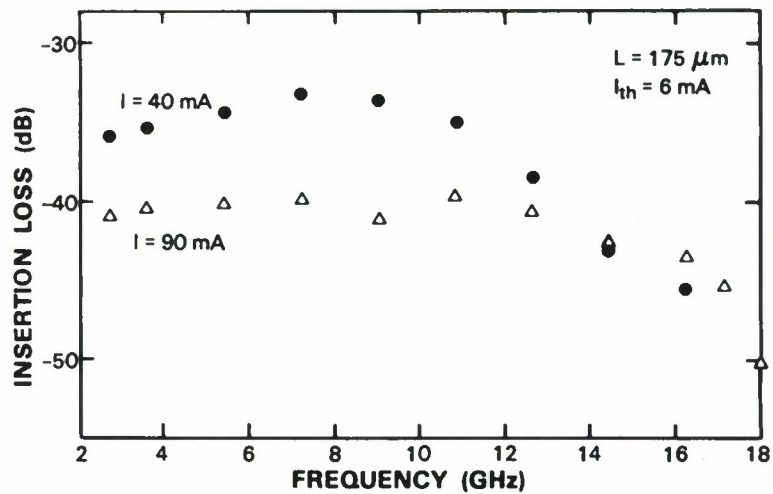
Figure 1-7. Frequency dependence of the insertion loss of the laser-photodiode optical link at laser bias currents of 40 mA and 90 mA.

A plot of the 3-dB roll-off frequency as a function of the square root of the optical power for the 16.4-GHz laser of Figure 1-7 is shown in Figure 1-8. The data are well behaved and follow a straight line with a slope of 5.5 GHz/mW$^{1/2}$. This slope is comparable to the slopes measured for n-substrate lasers of similar length[13] and for 100-μm-long n-substrate lasers with Zn-doped active regions.[12]
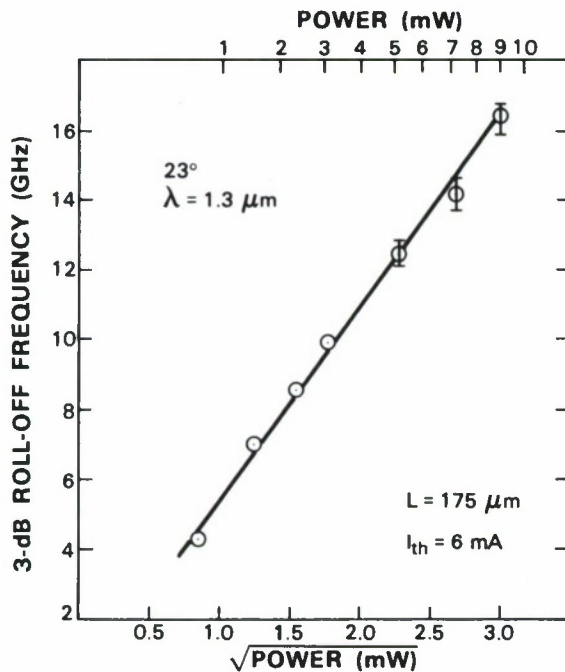
Figure 1-8. Three-dB roll-off frequency as a function of the square root of optical power.

8

The length of the p-substrate lasers investigated varied from 100 μm to 325 μm. Maximum frequency response was obtained for lasers with lengths of about 175 μm, which is similar to the results of Bowers[13] for n-substrate lasers. Long lasers ($>$200 μm) have high output power but intrinsically long photon lifetimes. Short lasers ($<$100 μm) have short photon lifetimes, but do not achieve sufficient output power because of strong nonlinear light-current characteristics at low current.

Near the roll-off frequency of the p-substrate lasers, a peak in the frequency response associated with the relaxation oscillation frequency can be observed. Similar to n-substrate lasers,[11-13] the frequency of this peak increases with bias and the relative magnitude decreases at high bias. Note, in Figure 1-7, that at 90 mA the peak virtually disappears and the response is flat to within 1 dB. These modulation characteristics of the p-substrate GaInAsP/InP lasers are comparable to the best characteristics observed for n-substrate lasers and make them attractive for high-speed systems.

D.Z. Tsang
Z.L. Liau

REFERENCES

1. T.E. Van Eck, P. Chu, W.S.C. Chang, and H.H. Wieder, Appl. Phys. Lett. **49**, 135 (1986).

2. J.Y. Marzin, M.N. Charasse, G. Le Roux, L. Goldstein, and M. Quillec, in *GaAs and Related Compounds 1984*, edited by B. de Cremoux (Adam Hilger, Bristol, England, 1985), pp. 373-378.

3. H. Asai and K. Oe, J. Appl. Phys. **54**, 2052 (1986).

4. S. Adachi, J. Appl. Phys. **53**, 8775 (1982).

5. S.P. Kowalczyk, W.J. Schaffer, E.A. Kraut, and R.W. Grant, J. Vac. Sci. Technol. **20**, 705 (1982).

6. P. Voisin, M. Voos, J.Y. Marzin, M.C. Tamargo, R.E. Nahory, and A.Y. Cho, Appl. Phys. Lett. **48**, 1476 (1986).

7. I.J. Fritz, B.L. Doyle, T.J. Drummond, R.M. Biefeld, and G.C. Osbourn, Appl. Phys. Lett. **48**, 1606 (1986).

8. J. N. Walpole and Z. L. Liau, Appl. Phys. Lett. **48**, 1636 (1986).

9. Z. L. Liau and J. N. Walpole, Appl. Phys. Lett. **46**, 115 (1985).

10. Z. L. Liau, J. N. Walpole, and D. Z. Tsang, IEEE J. Quantum Electron. **QE-20**, 855, (1984).

11. Solid State Research Report, Lincoln Laboratory, MIT (1985:2), p. 4, DTIC AD-A165692/5.

12. C. B. Su and R. Olshansky, Tech. Dig. Conf. Optical Fiber Communication (Atlanta, Georgia), February 1986, pp. 90-91.

13. J. E. Bowers, B. R. Hemenway, and A. H. Gnauck, IEEE J. Quantum Electron. **QE-22**, 833 (1986).

14. C. B. Su and V. Lanzisera, Appl. Phys. Lett. **45**, 1302 (1984).

15. C. A. Burrus, J. E. Bowers, and R. S. Tucker, Electron. Lett. **21**, 262 (1985). (We are grateful to C.A. Burrus and J.E. Bowers for the use of the InGaAs PIN detector.)

2. QUANTUM ELECTRONICS

2.1 SINGLE-FREQUENCY Ti:Al$_2$O$_3$ RING LASER

We previously have reported room-temperature CW operation of a Ti:Al$_2$O$_3$ laser with a maximum output power of 1.6 W at 770 nm.[1] Continuous tuning between 693 and 948 nm was achieved by using a Lyot filter in a folded three-mirror cavity.[2] We now have demonstrated single-frequency, tunable operation of a Ti:Al$_2$O$_3$ laser in a unidirectional ring cavity. A multiline Ar-ion laser is used to pump the laser rod. The CW output power at 12,985 cm^{-1} is 20 mW for an absorbed pump power of 2 W.

The 0.5-cm-long laser rod is cut from a Ti:A$_2$O$_3$ crystal grown by the seeded vertical gradient-freeze technique.[3] The faces of the rod are cut at the Brewster angle relative to the optic axis and are polished optically flat. At the peak of the Ti^{3+} pump band (490 nm), the absorption coefficient for the π polarization is 1.5 cm^{-1}, which indicates a composition of 0.048 wt% Ti in Al$_2$O$_3$.[4]

Figure 2-1 is a schematic of the four-mirror ring laser cavity. The pump radiation is injected into the cavity through one of the spherical mirrors. A lens of 17-cm focal length focuses the pump radiation into the Ti:Al$_2$O$_3$ rod, which absorbs about 50% of the incident radiation. The cavity folding angle at the spherical mirror is selected to compensate for the astigmatism introduced by the Brewster-cut rod.[5] The output coupler has 0.5% transmission. A broadband optical diode, a Lyot filter, and a 0.5-mm-thick etalon are placed inside the cavity. After each of these elements is inserted, the ring laser is realigned by adjusting the flat translating mirror.
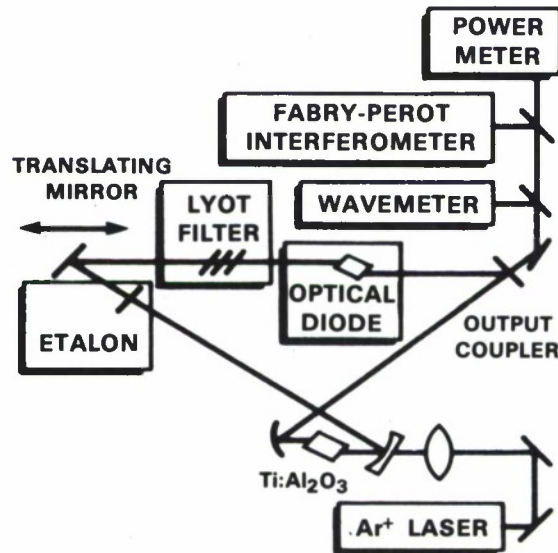
Figure 2-1. Schematic of the four-mirror ring cavity.

11

The frequency stability of the laser has been measured with a scanning Michelson wavemeter accurate to ±500 MHz and a scanning confocal Fabry-Perot interferometer with a free spectral range of 1.5 GHz. Over periods as long as an hour, no change in frequency was detected with the wavemeter. Figure 2-2 shows a typical trace for the transmission of the laser output through
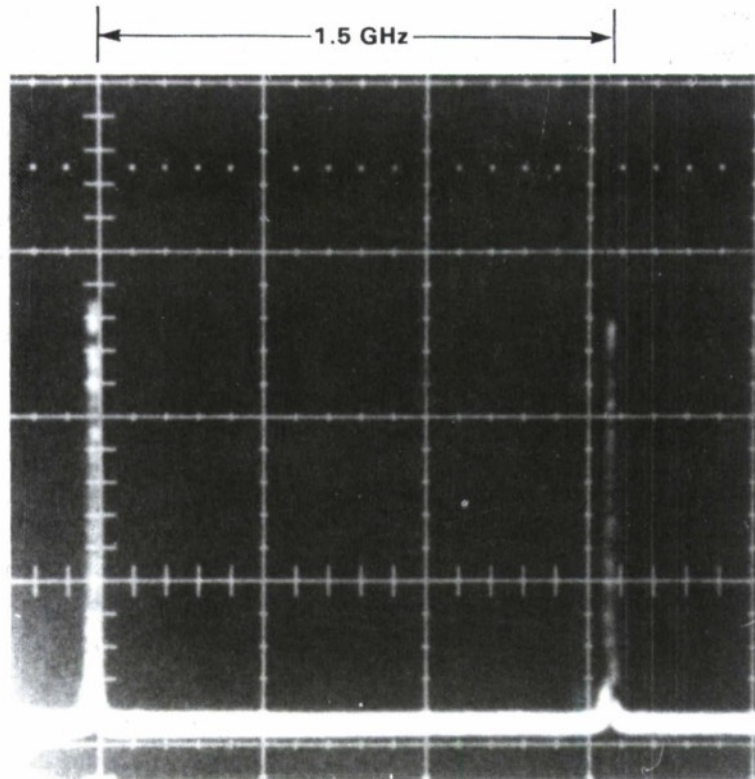
Figure 2-2.   Ring laser output, as observed with a scanning Fabry-Perot, shows single-frequency operation.

the Fabry-Perot. The measured linewidth is limited by the instrumental resolution, which is 30 MHz. However, over intervals of the order of one second the frequency exhibits fluctuations of as much as 250 MHz. These fluctuations, which are probably due to mechanical or thermal instabilities of the cavity, result in occasional mode hopping. The mode spacing is 290 MHz, consistent with the ring cavity length of 105 cm. An attempt is currently being made to reduce the cavity instabilities in order to improve the long-term frequency stability of the laser.

P.A. Schulz   R.E. Fahey
A. Sanchez   A.J. Strauss

2.2 EFFECT OF PHONON-ASSISTED UPCONVERSION ON 1.64-μm Er:YAG LASER PERFORMANCE

Previous experiments had shown that the performance of an Er:YAG laser was severely limited by a parasitic upconversion process that served to deplete the excited state population of Er ions in the $^4I_{13/2}$ level. Experiments now have been conducted that have measured the rate of the phonon-assisted (parasitic) upconversion process. This value has been incorporated in a rate equation analysis of the threshold and slope efficiency of an Er:YAG laser cavity and agrees with previous Er:YAG laser experiments.

The upconversion rate in Er:YAG was measured by using pulsed, 1.47-μm excitation and observing the temporal behavior of fluorescence emission at 1.64 μm from the $^4I_{13/2}$ level of Er. Figure 2-3 shows the experimental apparatus. An F-center laser was used to produce 30-ms,
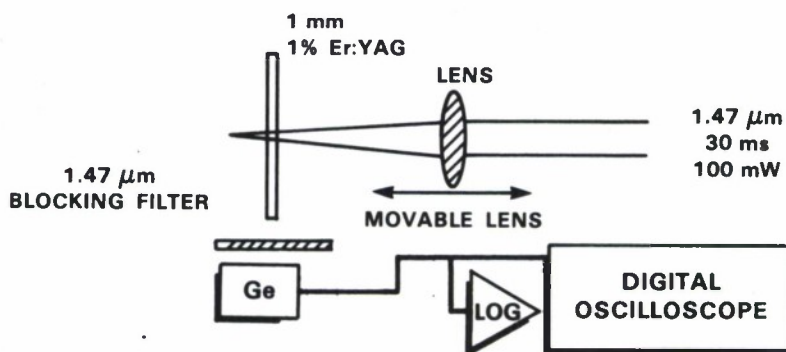
Figure 2-3. Schematic for transient analysis of Er:YAG fluorescence.

100-mW excitation radiation at one of the Er:YAG absorption lines near 1.47 μm, and then was focused by a 20-cm focal length lens onto a 1-mm-thick piece of 1% Er:YAG. The spacing between the Er:YAG crystal and the lens was variable in order to change the excitation intensity. Fluorescence emission near 1.64 μm from the $^4I_{13/2}$ level was detected by a germanium detector, processed by either a linear or logarithmic amplifier, and recorded by a digital oscilloscope. Figure 2-4 shows an oscilloscope trace of the fluorescence emission as the lens position was varied in order to vary the excitation intensity. Further analysis of the data showed that the decay rate of the fluorescence signal immediately following the excitation pulse increased by as much as a factor of 4 or 5 over the natural fluorescence decay rate. In addition, the fluorescence intensity decreased as the pump intensity increased even though the total excitation fluence was constant. Analysis of these temporal and intensity variations indicate that the upconversion rate constant, w_k, is approximately 1×10^{16} cm^{3}s^{-1}.

An analysis was made of the effect of the upconversion process on the threshold and slope efficiency of the Er:YAG laser cavity. Figure 2-5 shows the appropriate energy levels involved in

13

LOW INTENSITY

LOG (Fluorescence)

LINEAR (Fluorescence)
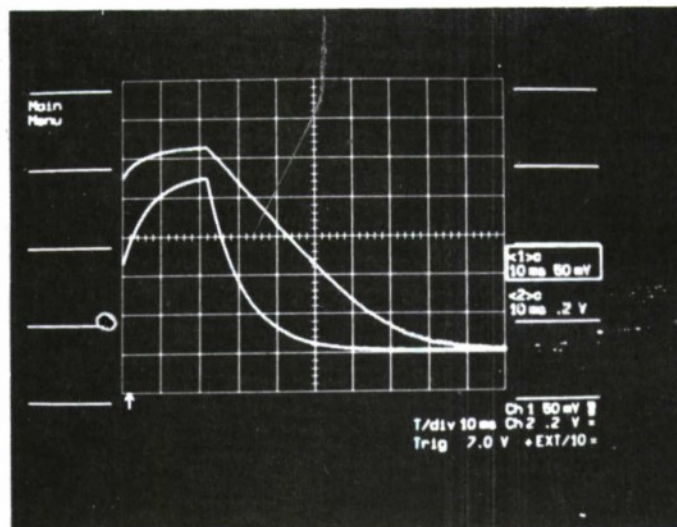
HIGH INTENSITY

LOG (Fluorescence)

LINEAR (Fluorescence)
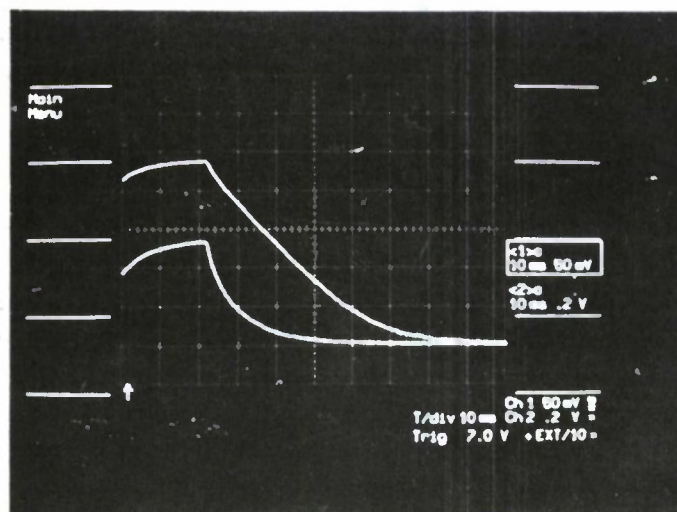
Figure 2-4. *Temporal display on an oscilloscope of the 1.65-μm fluorescence from Er:YAG as 1.47-μm excitation intensity was varied.*

14
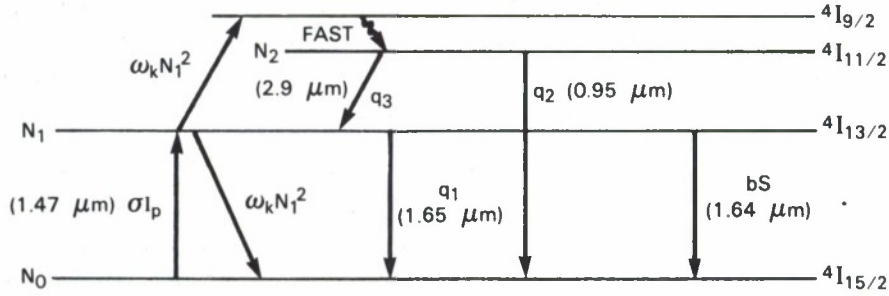
Figure 2-5. Energy levels and transitions involved in rate equation analysis of Er:YAG laser cavity.

the Er:YAG laser. N_0, N_1, and N_2 are the population densities of the manifolds shown. The rate equations may be written by inspection of Figure 2-5 and, as examples, two of the equations are given by

$$\frac{dN_0}{dt} = - \alpha\sigma I_p N_0 + (\sigma\beta I_p + q_1)N_1 + q_2 N_2 + w_k N_1^2 + bS(\gamma N_1 - \delta N_0) \qquad (2\text{-}1)$$

and

$$\frac{dS}{dt} = Sbc\,(\gamma N_1 - \delta N_0) - \frac{S}{\tau_c} \qquad (2\text{-}2)$$

where I_p is the 1.47-μm pump laser intensity; σ is the absorption cross section, w_k is the upconversion rate, and b is the emission cross section at the laser transition (1.64 μm); q_1, q_2, and q_3 are the radiative decay rates of the levels shown; and α, β, γ, and δ are the appropriate Boltzmann population factors within the N_0 and N_1 levels. S is the 1.64-μm laser intensity in the cavity. The cavity lifetime, τ_c, equals $\ell/c(1 - R)$, where R is the reflectivity of the cavity mirrors and ℓ is the cavity length.

One sees by inspection of the above equations that, under steady state laser operation, the population inversion density is clamped at a value of $(1 - R)/b\ell$. Under these conditions, the population density N_1 is given approximately by $T(\delta/\gamma) + (1 - R)/(\gamma b\ell)$, where $T = N_0 + N_1 + N_2$ is the total density of Er ions (i.e., 1.4×10^{20} ions/cm^3 for 1% Er doping). Solving the above equations for the steady state solution, one can show that the laser intensity out of the cavity, $S(1 - R)$, may be given as

$$S(1 - R)\,(L/\ell) = I_p\left[1 - \frac{\sigma\alpha w_k N_1^2 L}{(q_1 + q_3)}\right] - \left\{N_1 q_1 L + N_1^2 L\left[2\omega k - \frac{q_3 w_k}{q_2 + q_3}\right]\right\} \quad . \qquad (2\text{-}3)$$

L is the active excitation length in the crystal, where $L \approx [\sigma\alpha\,(T - N_1)]^{-1}$. The bracketed term is the slope efficiency of the laser, and the braced term is the laser threshold. As can be seen, both terms are influenced by the upconversion term, w_k.

One can compare the predicted laser behavior of Equation (2-3) with past Er:YAG laser experiments. Previous experiments had shown that the Er:YAG laser threshold was approximately a factor of 10 higher than expected. Using this factor for the ratio of the

15

upconversion threshold term in Equation (2-3) compared to the normal threshold value, $N_1 q_1$, one deduces that $w_k = 3 \times 10^{16}$ cm^{3}s^{-1}, in good agreement with the previous experimental results. As can be seen from these results, the upconversion process is, unfortunately, an effective channel for the depletion of the population inversion between N_1 and N_0.

It should be noted that while the above analysis indicates that upconversion is a serious detriment for the use of Er:YAG as a laser source at 1.64 μm, it is beneficial for operation of the Er:YAG laser at 2.9 μm since in this case it effectively de-excites the lower laser level. In addition, it may be possible to use the upconversion process to obtain visible (0.53 μm) or near IR (0.95 μm) laser radiation directly. Additional experiments are planned to investigate these possibilities.

D.K. Killinger

2.3 Nd:YAG SUM-FREQUENCY GENERATION OF SODIUM RESONANCE RADIATION

Sodium resonance radiation has been generated by sum-frequency mixing the output radiation of two CW Nd:YAG lasers that each contained an intracavity etalon for wavelength tuning, as shown schematically in Figure 2-6. One Nd:YAG laser operated at a wavelength of 1.0642 μm and produced 1 W of TEM$_{oo}$ power within a spectral linewidth of 340 MHz. The other Nd:YAG laser operated at a wavelength of 1.3189 μm and produced 300 mW of TEM$_{oo}$ power within a spectral linewidth of 220 MHz. The two Nd:YAG laser beams were aligned coaxially using a dichroic mirror and then focused into a 5-cm-long lithium niobate crystal that was heated to a temperature of 240 $\pm$ 10°C. Approximately 0.2 mW of sum radiation was generated in the crystal. The relative temperature dependence of the sum-frequency intensity is illustrated in Figure 2-7.
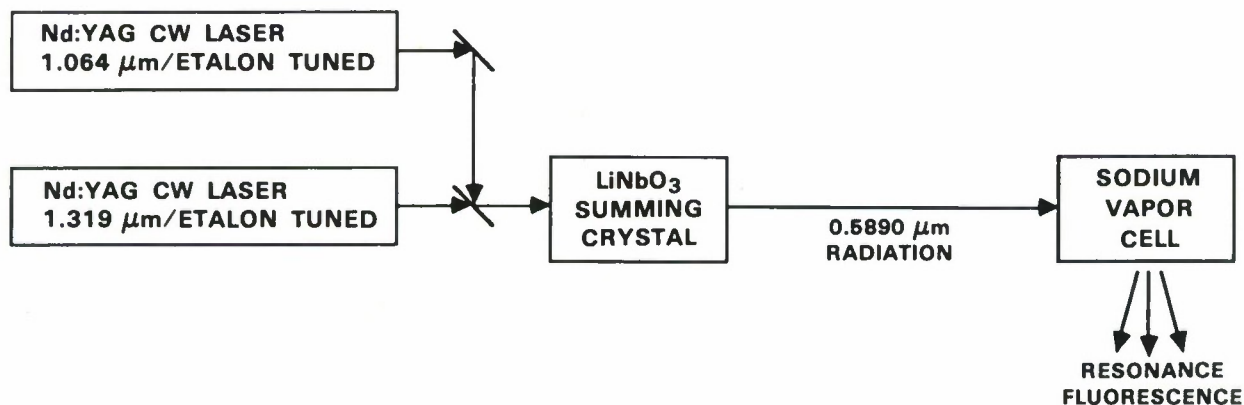
Figure 2-6. Schematic showing the sum-frequency generation of sodium resonance radiation by combination of 1.064-μm and 1.319-μm CW laser radiation in a lithium niobate mixing crystal.
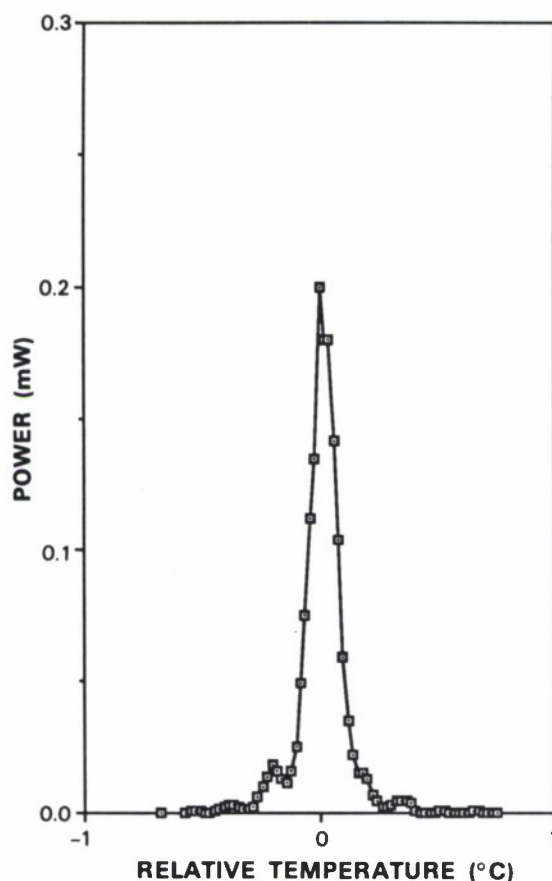
Figure 2-7. *Sum radiation intensity as a function of the relative temperature of the lithium niobate mixing crystal. The absolute error in the intensity measurement is approximately 50%.*

The sum wavelength could be tuned over a 1.5 Å range in the vicinity of 0.589 μm. This tuning was accomplished by tilting the solid etalons within each of the Nd:YAG lasers in conjunction with temperature adjustment of the lithium niobate crystal. The Nd:YAG rods were operated with a water coolant temperature of about 30°C in order to shift the center of the 1.064-μm line.[6] The sum radiation had a linewidth of 380 MHz, as shown in Figure 2-8, which is much narrower than the 3-GHz Doppler broadened sodium absorption linewidth. When tuned to the sodium D_2 transition, the sum radiation was observed to be completely absorbed in a high density (10^{11} atoms/cm^3) sodium cell. Further experiments are planned to better match the sum-radiation linewidth to the sodium absorption linewidth by phase modulating the Nd:YAG laser radiation both intracavity and extracavity.

T.H. Jeys
D.K. Killinger
A.A. Brailove

17
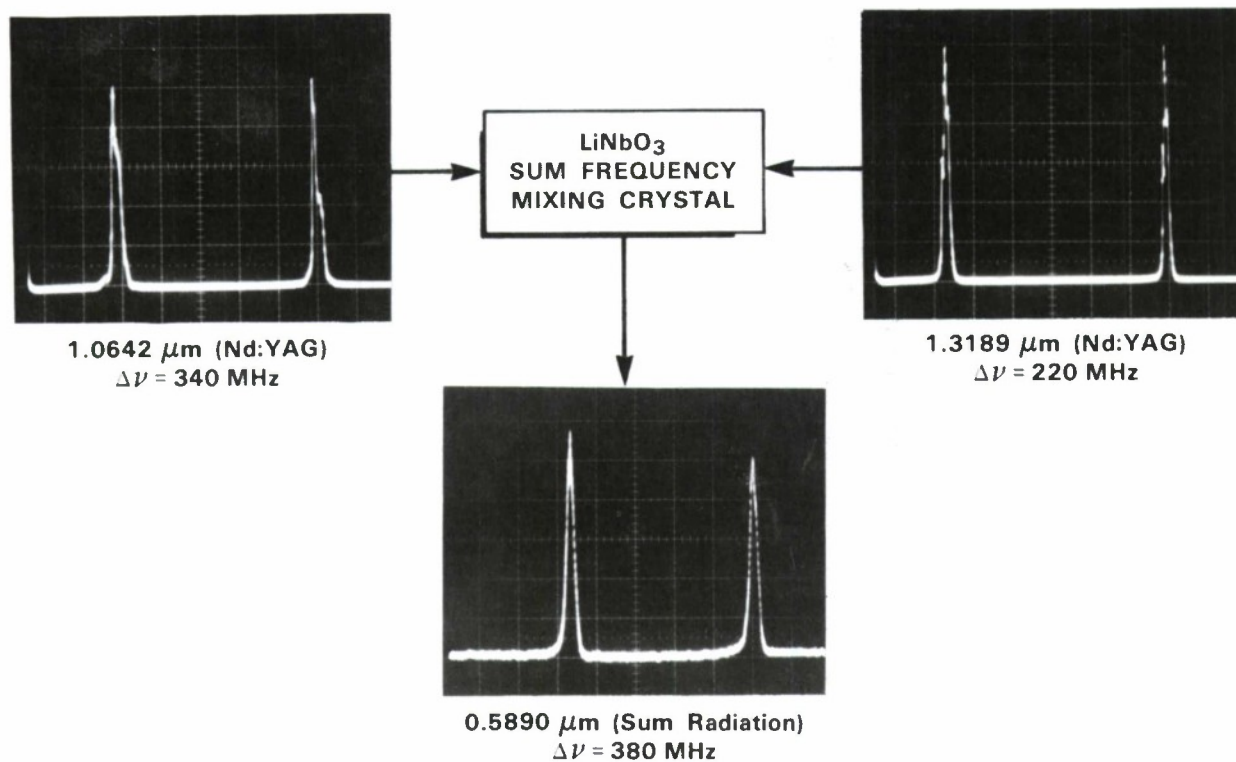
Figure 2-8. Spectral lineshapes of the 1.0642-μm, 1.3189-μm, and 0.5890-μm radiation as measured by three separate scanning confocal etalons. Each etalon has a free spectral range of 8.0 GHz, which is represented by the distance between the repeated spectral peaks on each oscilloscope trace.

2.4 OBSERVATION OF THE STARK EFFECT ON EXCITONIC STATES IN AlGaAs/GaAs COUPLED QUANTUM WELLS

AlGaAs/GaAs coupled quantum wells (CQW) have been grown in the insulating region of a PIN structure, as illustrated in Figure 2-9. The confined excitonic states of the CQW were studied as a function of voltage applied to the device, using luminescence-excitation spectroscopy and reflectivity. One set of luminescence-excitation data is shown in Figure 2-10. The most salient features in the observed spectra, besides the abundance of spectral lines, are the crossings of several levels, the linear Stark shift, and the overall sensitivity of the spectra with respect to applied bias. The observed peak shifts are traced out as a function of bias in Figure 2-11. Line shifts of more than 10 meV are observed with a bias of less than 2 V, corresponding to an estimated internal electric field of about 10^4 V/cm. In addition, the oscillator strengths associated with the levels also vary greatly.

The observed features are uncharacteristic of single quantum well systems, but are understood readily with a CQW model. The theory used ignores the differences in the excitonic binding energies of various states with different CQW envelope wave functions, and approximates

18

GaAs SUBSTRATE
AND BUFFER

0.8 μm p$^+$ AlGaAs SL

0.1 μm i Al$_{0.2}$Ga$_{0.8}$As

25 PERIODS
{ 11 nm GaAs
2 nm Al$_{0.2}$Ga$_{0.8}$As
7.5 nm GaAs

0.1 μm i Al$_{0.2}$Ga$_{0.8}$As

0.35 μm n$^+$ AlGaAs SL

n$^+$GaAs

(a)

n$^+$ hν V$_{bias}$

i

p$^+$

(b)
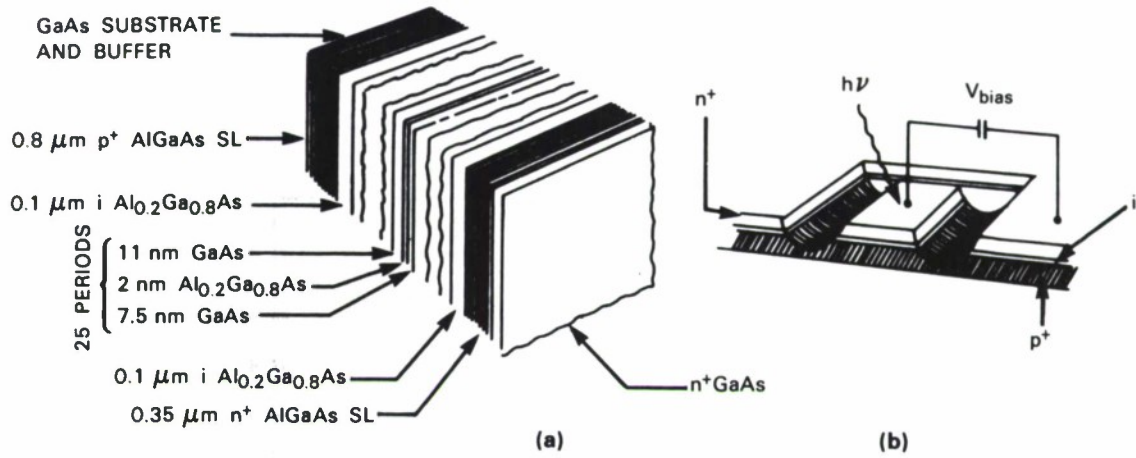
Figure 2-9.   Coupled quantum well sample diagram showing (a) cross section through quantum well region, and (b) back-to-back PIN diode structure used in measurements. Drawing is not to scale.

the hole 3/2-spinor with two scalar particles. Despite the approximations, the major features of the experimental results are accounted for. Figure 2-12 shows the calculated energies of the various transitions as a function of applied electric field. The transitions are labeled according to the bands involved, with e, h, and l denoting electron, heavy-hole and light-hole states; and subscripts 1 and 2 referring to the lowest and next to lowest energy levels.

H.Q. Le   W.D. Goodhue
J.J. Zayhowski   J.W. Bales

19
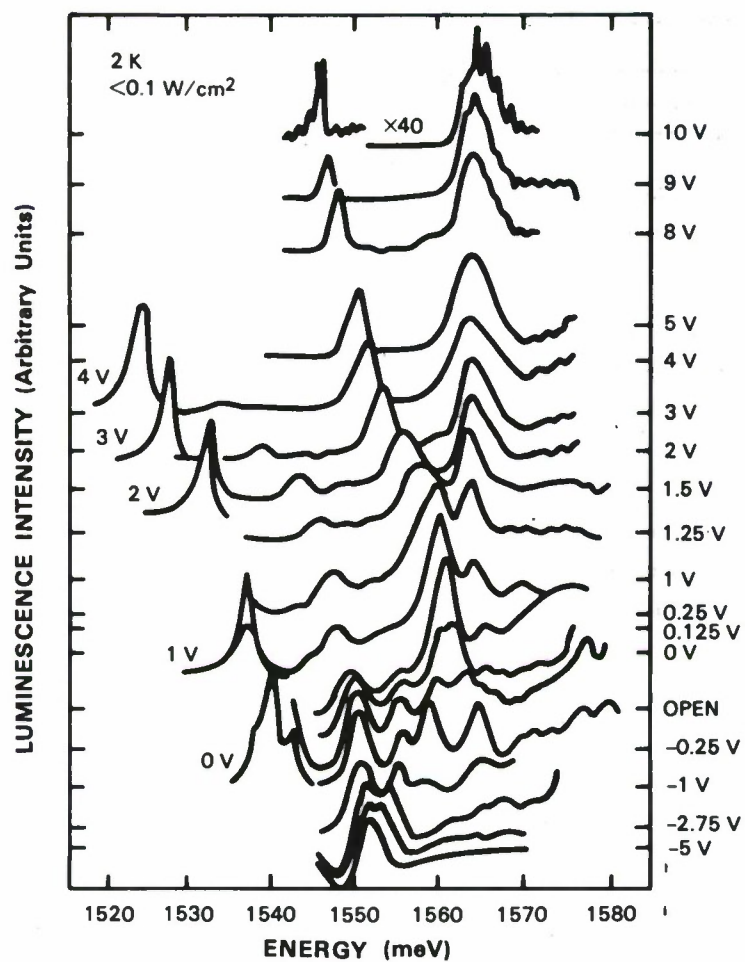
Figure 2-10. Excitation and luminescence spectra for different bias voltages. Traces marked from 0 V to 4 V are luminescence spectra. All others are excitation spectra. Right vertical labels denote the applied voltages, arranged in the same vertical order as the associated traces.
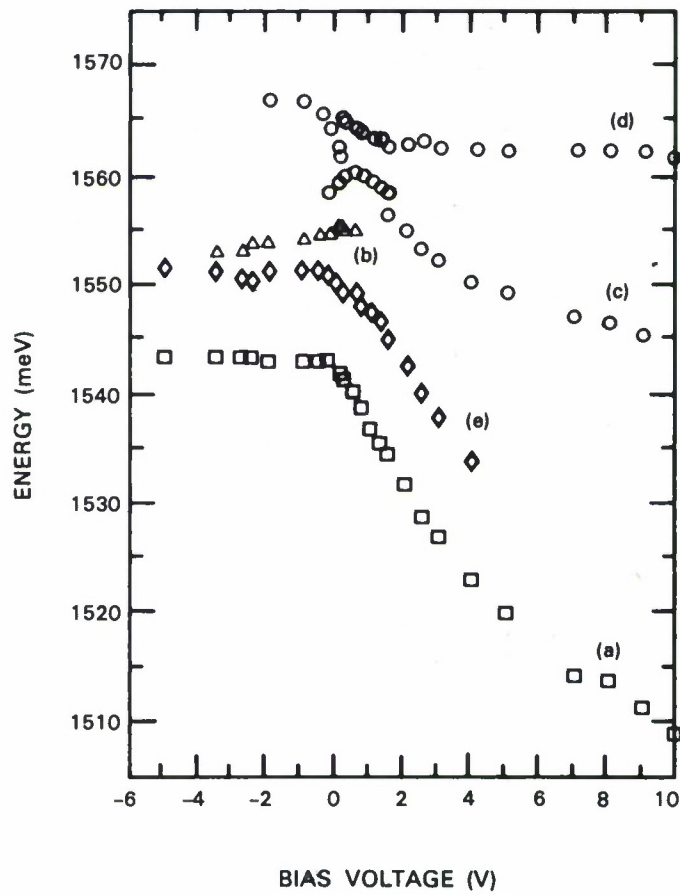
Figure 2-11. Observed peak shifts vs applied voltage. Different symbols are used to help distinguish well-traced peaks.

21
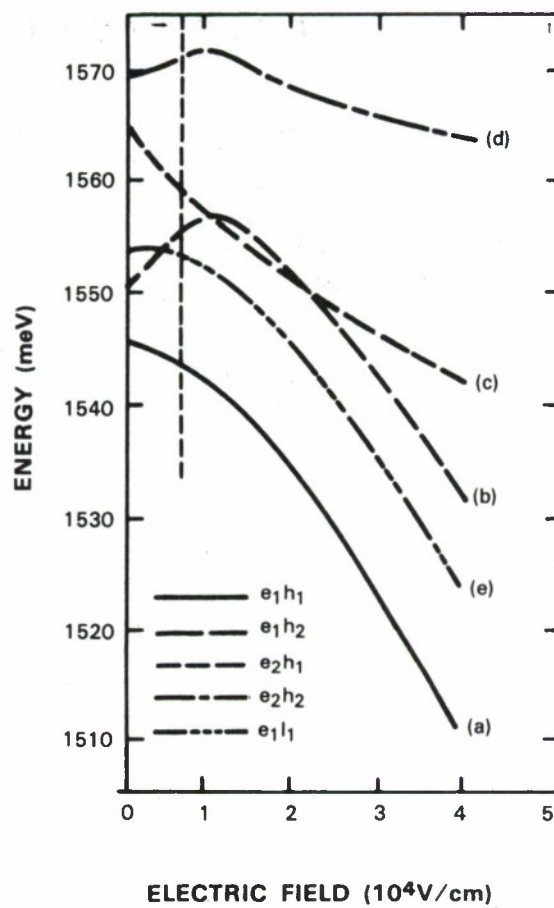
Figure 2-12. Calculated Stark shift of CQW states. Traces (a), (b), (c), (d), and (e) correspond to transitions (e_1, h_1), (e_1, h_2), (e_2, h_1), (e_2, h_2) and (e_1, l_1), respectively.

REFERENCES

1. A. Sanchez, R.E. Fahey, A.J. Strauss, and R.L. Aggarwal, Opt. Lett. **11**, 363 (1986).

2. A. Sanchez, R.E. Fahey, A.J. Strauss, and R.L. Aggarwal, Proc. Topical Meeting on Tunable Solid State Lasers, Zigzag, Oregon, 4-6 June 1986.

3. A.J. Strauss, R.E. Fahey, A. Sanchez, and R.L. Aggarwal, SPIE Proc., Vol. 681, 1986 (to be published).

4. R.L. Aggarwal, A. Sanchez, R.E. Fahey, and A.J. Strauss, Appl. Phys. Lett. **48**, 1345 (1986).

5. H.W. Kogelnik, E.P. Ippen, A. Dienes, and C.V. Shank, IEEE J. Quantum Electron. **QE-8**, 373 (1972).

6. T. Kushida, Phys. Rev. **185**, 500 (1969).

3. MATERIALS RESEARCH

3.1 RADIATION-HARDENED Si-ON-INSULATOR JFETs FABRICATED BY A SELF-ALIGNED PROCESS

A self-aligned process has been developed for fabricating junction field-effect transistors (JFETs) in silicon-on-insulator (SOI) films prepared by zone-melting recrystallization (ZMR) using the graphite-strip-heater technique. This process has been used to fabricate n-JFETs exhibiting high transconductance, low output conductance, and good threshold voltage uniformity. Excellent radiation resistance up to 10^8 rad(Si) has been observed with respect to threshold voltage and transconductance.

Because the JFET structure has no gate oxide, JFETs are inherently less sensitive to total-dose radiation than MOSFETs. In MOSFETs, charge trapping in the gate oxide during irradiation generally produces a large shift in threshold voltage. Although we have achieved[1] total-dose resistance up to 10^7 rad(Si) for SOI/CMOS devices by using a gate oxide only 10 nm thick, it would be very difficult to extend the radiation hardness of such devices to higher total-dose levels, since this would require still thinner oxide. We have reported[2] previously the fabrication in SOI films of complementary JFETs exhibiting excellent total-dose radiation hardness up to 10^8 rad(Si). However, because these devices were not self-aligned, they had relatively high source and drain parasitic resistance, resulting in low dc transconductance and limited output driving capability.

We now have fabricated self-aligned n-JFETs in 0.5-μm-thick SOI films prepared by ZMR[3] on 1-μm-thick SiO_2 layers on Si substrates. Figure 3-1 is a schematic diagram of the device structure. A coplanar LOCOS process was used for device isolation. A back-channel implantation was performed with boron to insure uniformity in channel height despite slight local variations in SOI film thickness. Arsenic was implanted to form two closely spaced n regions above the
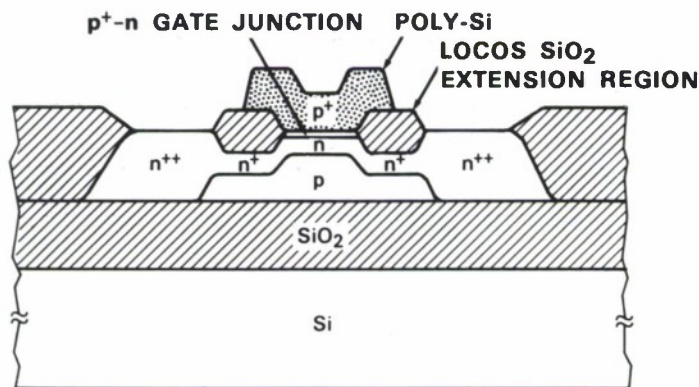
Figure 3-1.   Schematic device structure of self-aligned SOI n-JFET.

25

boron-implanted p layer. The device channel was defined by forming a LOCOS-oxide extension region above each of the n regions. The arsenic doping below the LOCOS oxide was sufficient to reduce the source and drain resistance without degrading gate junction quality. The channel implantation then was performed with arsenic. Poly-Si was deposited and doped p$^+$ by implanting with a heavy dose of boron. The gate area was defined by a combination of dry and wet etching. The gate junction was formed by diffusion from the doped poly-Si gate, producing a shallow junction. The n$^+$ source and drain were formed by phosphorus implantation, using the LOCOS-oxide extension regions and poly-Si gate for masking. Thus, the source and drain are self-aligned with respect to the oxide extension regions. The dose used for poly-Si doping was high enough compared to the source/drain dose to insure low resistivity in the poly-Si gate. The nominal gate width is 30 μm, the gate length is 2 μm, and the source-drain spacing is 6 μm.

Figure 3-2 shows the transistor characteristics of a self-aligned n-JFET. The threshold voltage is about 0.6 V, compared with the desired value of 0.1 V for an enhanced-mode JFET. The transconductance measured at V_{gs} = 1-2 V is about 55 mS/mm. The highest transconductance measured for any of the devices is about 63 mS/mm. Unlike SOI n-MOSFETs, SOI JFETs do not show kinks in their transistor characteristics. The output conductance, which is as low as 0.4 mS/mm at a drain current of 400 μA, is roughly inversely proportional to the square root of the drain current. The leakage current is relatively high because the edge of the channel under the LOCOS oxide is not effectively controlled by the gate potential. The edge leakage current can be eliminated by a small change in processing.
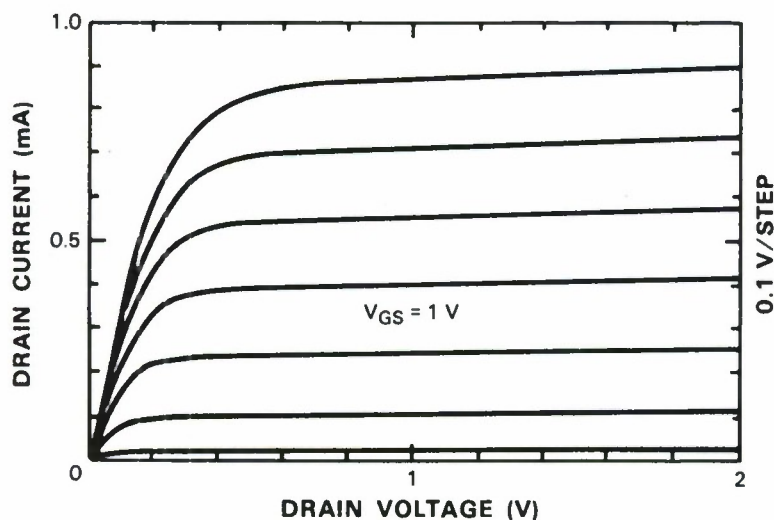
Figure 3-2. Transistor characteristics of self-aligned SOI n-JFET. The nominal gate length is 2 μm and the gate width is 30 μm.

26

In order to investigate whether the self-aligned processing procedure is suitable for large-scale circuit fabrication, the threshold voltage distribution was measured. Figure 3-3 shows this distribution for 228 transistors within an area of about 4×4 cm^2. The mean is 578 mV and the standard deviation is 22 mV. Although the data are preliminary, this deviation compares favorably with the best values obtained in GaAs MESFET technology.
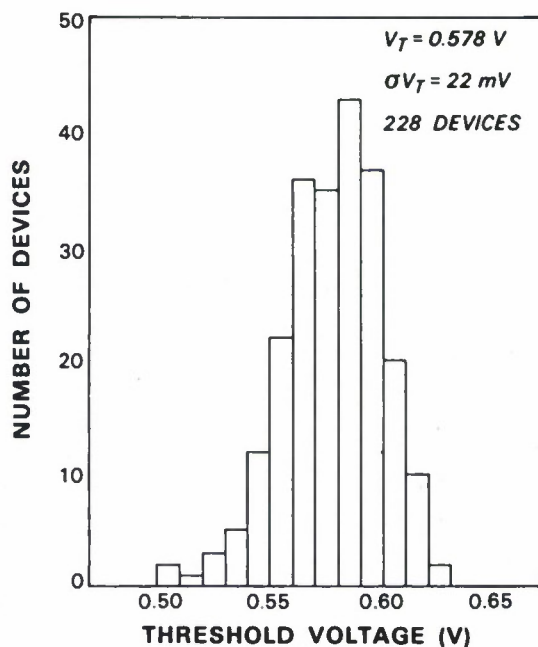
Figure 3-3.   Distribution of threshold voltage for self-aligned JFETs.

The JFETs were mounted in ceramic packages without covers and irradiated with a beam of 1.5-MeV electrons from a Van de Graaff accelerator. The bias voltages during irradiation were: gate voltage V_G and drain voltage $V_D = 0$ or 1.5 V and substrate voltage $V_B = -15$ V. A negative substrate bias was found to be important in reducing the threshold voltage shift with radiation.[2] Measurements of threshold voltage and transconductance were performed within 10 min after exposure.

Figure 3-4 shows the threshold voltage shift as a function of ionizing dose from 5×10^4 to 10^8 rad(Si) for three different pairs of V_D and V_G values. For all bias conditions, the threshold voltage shift becomes increasingly negative up to 5×10^7 rad(Si) and recovers slightly at 10^8 rad(Si). Under the worst bias condition, the maximum shift in threshold voltage is less than

27
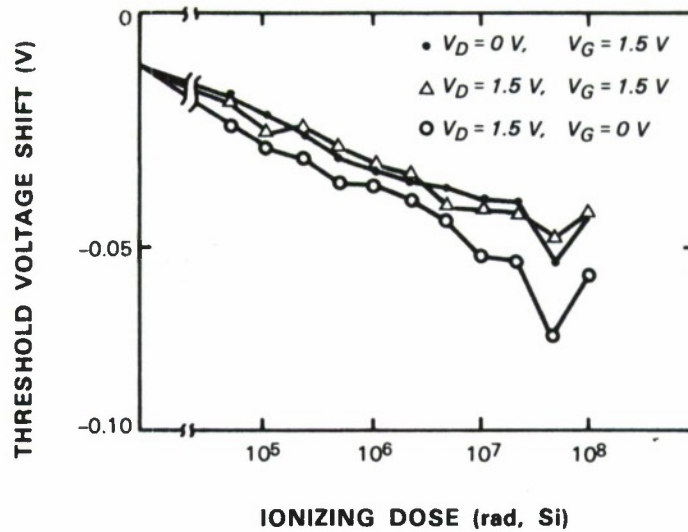
Figure 3-4. Threshold voltage shifts of self-aligned JFETs as a function of ionizing dose. The bias voltages during irradiation are shown in the figure.

75 mV. The transconductance is virtually constant up to 10^5 rad(Si) and then decreases monotonically. The decrease in transconductance, which is only about 30% at 10^8 rad(Si), is due to carrier mobility degradation.

H.K. Choi
B-Y. Tsaur
C.K. Chen

3.2 GaAs/AlGaAs DOUBLE-HETEROSTRUCTURE DIODE LASERS ON (110) GaAs SUBSTRATES

There has been no previous report of GaAs/AlGaAs heterostructure devices fabricated on (110) GaAs substrates, apparently because of the difficulty encountered in growing device-quality epilayers with this orientation. Here we report the first (110) GaAs/AlGaAs diode lasers, which have been fabricated in double heterostructures (DH) grown by organometallic vapor phase epitaxy (OMVPE) on substrates oriented 2° off (110) toward (11$\bar{2}$). These devices have characteristics comparable to those reported for lasers with similar structures on (100) substrates.

Our work on (110) diode lasers has been motivated by their potential for utilization in monolithic two-dimensional surface-emitting laser arrays. Such arrays can be fabricated from edge-emitting devices having etched facets that are coupled with mirrors deflecting the laser radiation by 90° so that it emerges normal to the wafer surface.[4,5] For (110) substrates, there are {111} planes that are normal to the substrate surface. Since (111A) and (111B) are, respectively, the slowest and fastest etching planes for many wet-chemical etchants, facet-deflector pairs can be obtained by wet-chemical etching.

28

The GaAs and AlGaAs layers were grown in a horizontal OMVPE system at atmospheric pressure on GaAs substrates slightly misoriented from the (110) plane. Trimethylgallium and trimethylaluminum were used as the Ga and Al sources and arsine as the As source. The surface morphology of the epitaxial layers was very sensitive to the direction of substrate misorientation. Figure 3-5 shows Nomarski photographs of GaAs layers grown at 780°C, with a V/III ratio of about 60, on substrates tilted 2° toward (1$\bar{1}$0), (1$\bar{1}$2) or (1$\bar{1}$2). (For convenience, in the following discussion the (1$\bar{1}$2) and (1$\bar{1}$2) planes will be designated as (112A) and (112B), respectively.) The best surface morphology was obtained when the substrate was tilted toward (112A).
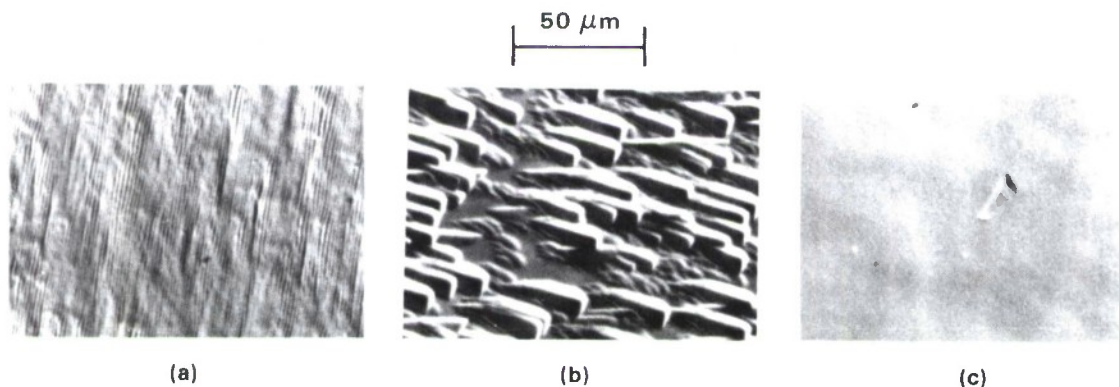
Figure 3-5. *Nomarski photomicrographs showing the surface morphology of GaAs grown on substrates oriented (a) (110) → (110), (b) (110) → (112B), and (c) (110) → (112A). The substrate temperature was 780°C.*

The quality of the layers of Figure 3-5 was characterized by photoluminescence (PL) measurements at 5 K. Figure 3-6 shows the PL spectra excited by an Ar-ion laser emitting at 647 nm with a power density of about 7.5 W/cm^2. The strongest and sharpest exciton peak was obtained for the layer grown on the substrate tilted toward (112A). By reducing the power density to 0.75 W/cm^2, we could resolve the free, donor-bound and acceptor-bound exciton peaks, indicating the high purity and crystal quality of this layer. Because both the smoothest morphology and strongest PL were obtained for (110) tilted toward (112A), further experiments were confined to this orientation.

The GaAs layers were much less sensitive to substrate temperature and V/III ratio than to orientation. The surface morphology was not much changed for substrate temperatures up to 820°C, but the surface was slightly rougher for growth at 850°C. In contrast, the surface morphology of AlGaAs layers was very sensitive to the substrate temperature. The most serious problem was large surface defects, as shown in Figure 3-7(a) for a layer grown at 820°C with a V/III ratio of about 30. The size of the defects was fairly uniform, indicating that they originated from the substrate. The density of these defects increased with decreasing substrate temperature. The density was significantly reduced by *in situ* HCl etching prior to growth. Under optimum

29
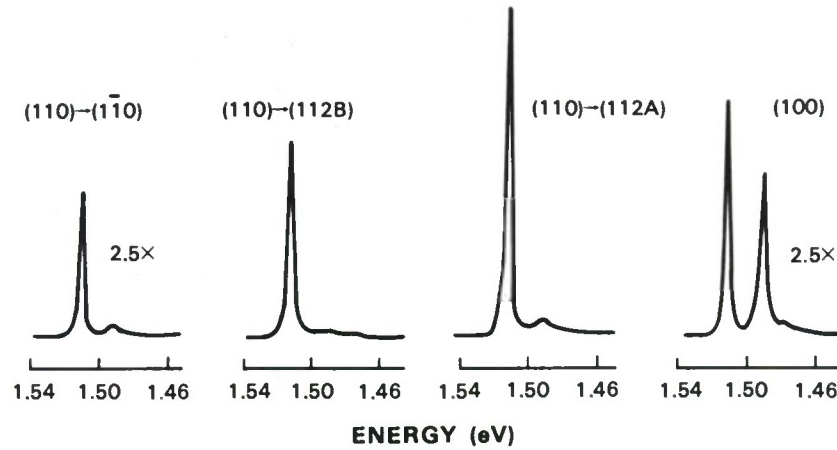
Figure 3-6. *Low-temperature photoluminescence (PL) spectra of GaAs layers grown on substrates oriented (a) (110) → (110), (b) (110) → (112B), (c) (110) → (112A), and (d) (100).*
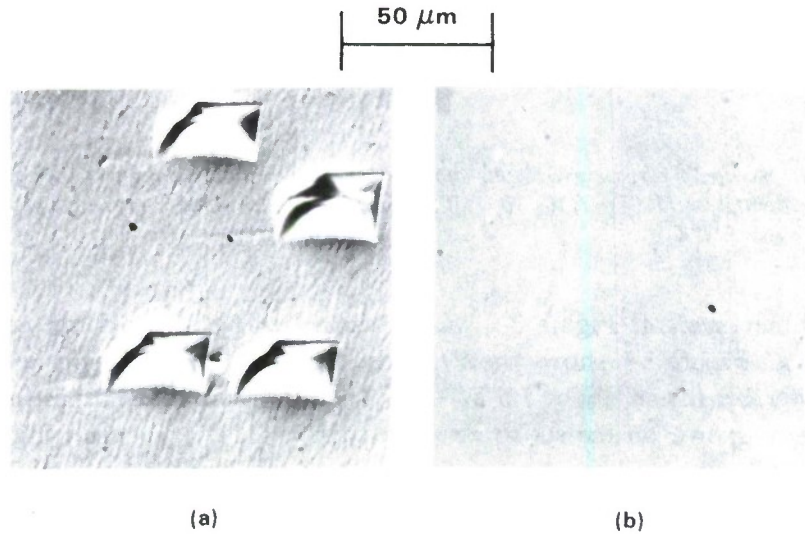
Figure 3-7. *Nomarski photomicrographs showing the surface morphology of AlGaAs grown at substrate temperatures of (a) 820° C, and (b) 850° C. The substrate orientation was (110) → (112A).*

conditions, AlGaAs with very smooth morphology and few defects could be obtained at a substrate temperature of 850°C, as shown in Figure 3-7(b). Figure 3-8 shows the low-temperature PL spectra of an $Al_{0.28}Ga_{0.72}As$ layer excited by an Ar-ion laser at 568 nm with power densities of 7.5 and 30 W/cm^2. Both an exciton peak and strong carbon peak are observed.

A DH laser structure consisting of the following layers was grown at 850°C on a GaAs substrate oriented 2° off (110) toward (112A): 1-μm-thick n $Al_{0.28}Ga_{0.72}As$ confinement,
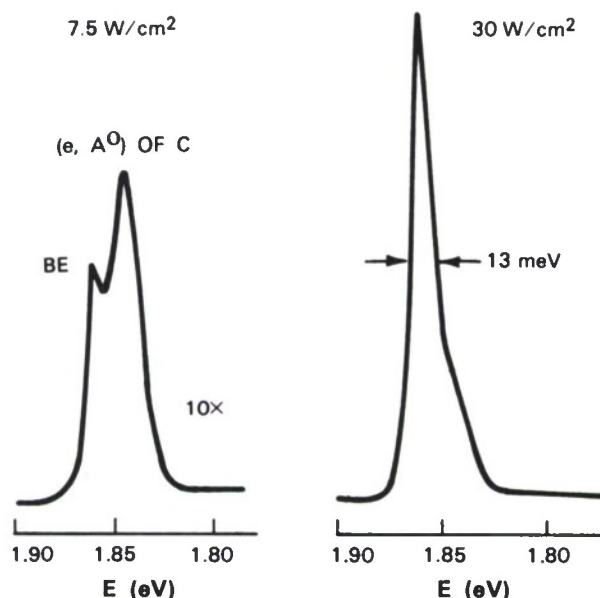
Figure 3-8. Low-temperature PL spectra of $Al_{0.28}Ga_{0.72}As$ for excitation power densities of 7.5 and 30 W/cm^2.

0.1-μm-thick nominally undoped GaAs active, 1-μm-thick p $Al_{0.28}Ga_{0.72}As$ confinement, and 0.2-μm-thick p+ GaAs cap. Broad-area lasers were fabricated with cleaved facets. Figure 3-9 shows the pulsed threshold current density J_{th} as a function of cavity length L. The lowest J_{th} for L = 350 μm was 730 A/cm^2, which approximates the lowest values reported for lasers of similar structure on (100) substrates.

Oxide-defined stripe-geometry lasers with a stripe width of 6 μm also were fabricated. Figure 3-10 shows the current vs light output characteristic of a laser with L = 210 μm that was operated with 100-ns pulses at a duty cycle of 0.1%. The threshold current was 60 mA, and the differential quantum efficiency was 33% per facet. Light output of more than 20 mW was obtained without kinks for many of the lasers, indicating uniform material quality. Figure 3-11 shows the data for threshold current as a function of L, together with data reported[6] for DH stripe-geometry lasers with an $Al_{0.07}Ga_{0.93}As$ active region and $Al_{0.45}Ga_{0.55}As$ confinement layers that were grown by OMVPE on (100) substrates. For the same cavity length, the threshold current of the (110) lasers was about 20 mA higher than that of the (100) lasers. However, the AlAs mole fraction difference between the active and confinement layers is 0.38 for the (100) lasers and only 0.28 for (110) lasers. For the same difference in AlAs mole fraction, the difference in threshold current should be much smaller.

In order to demonstrate the potential usefulness of (110) lasers for monolithic two-dimensional surface-emitting arrays, facet-deflector pairs were formed by wet-chemical etching of a DH consisting of the following layers grown by OMVPE: 1-μm-thick n AlGaAs,

31
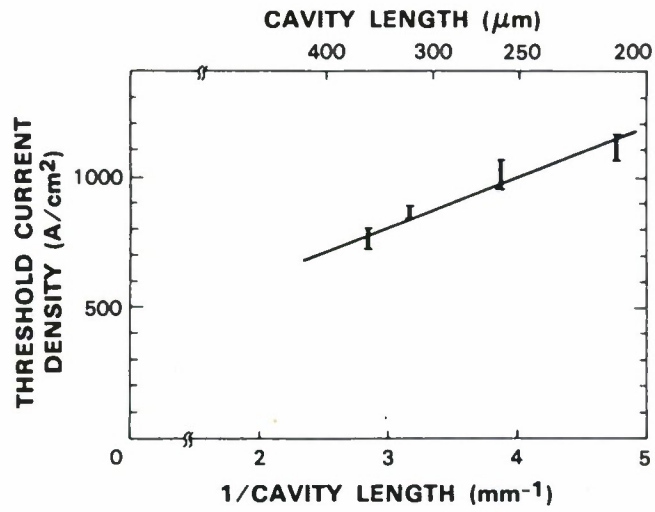
Figure 3-9.   Threshold current density as a function of cavity length for broad-area (110) DH diode lasers.
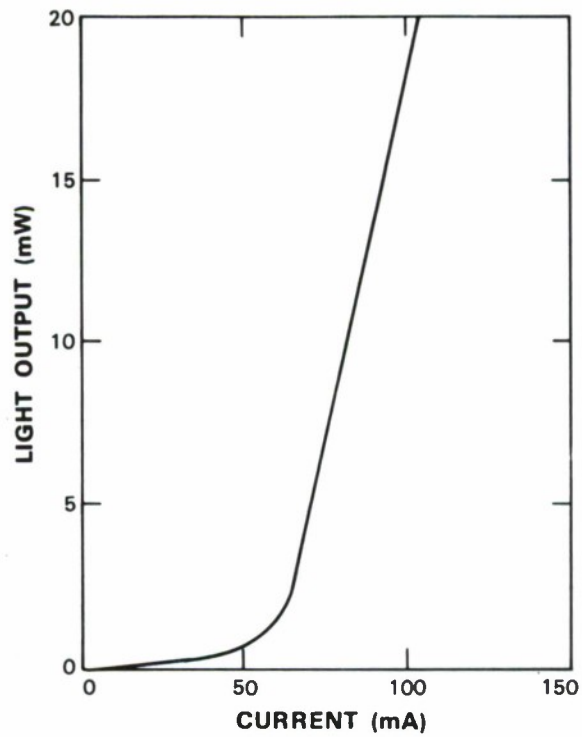
Figure 3-10.   Light output vs current for a stripe-geometry (110) DH laser. The threshold current is 60 mA, and the differential quantum efficiency is 33% per facet.

32
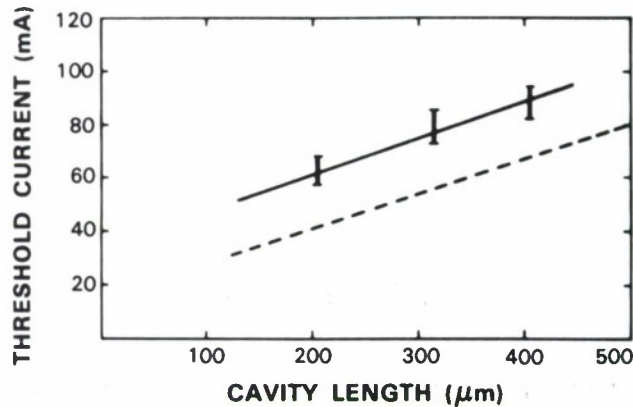
Figure 3-11. Threshold current as a function of cavity length for stripe-geometry (110) DH lasers. The dotted line represents data reported in Reference 7 for $Al_{0.07}Ga_{0.93}As/Al_{0.45}Ga_{0.55}As$ DH lasers.

0.1-μm-thick GaAs, 3-μm-thick p AlGaAs, and 0.2-μm-thick p+ GaAs. Silicon dioxide was deposited on the wafer, stripes 2 μm wide were opened perpendicular to the [111] direction, and the sample was etched with Br:CH$_3$OH. Figure 3-12 is a scanning electron micrograph showing a facet-deflector pair in cross section. In the (111A) direction, a vertical facet was obtained because the (111A) plane is the slowest etching plane. However, since there is no slow etching plane in the opposite direction, the profile of the opposite wall was determined by etchant diffusion, resulting in a semicircular shape. The facet and deflector surfaces were both very smooth. In order to complete laser fabrication, it would be necessary to form the other facet by a dry etching technique such as reactive-ion or ion-beam-assisted etching.

<div style="text-align:right">

H.K. Choi
M.K. Connors

</div>
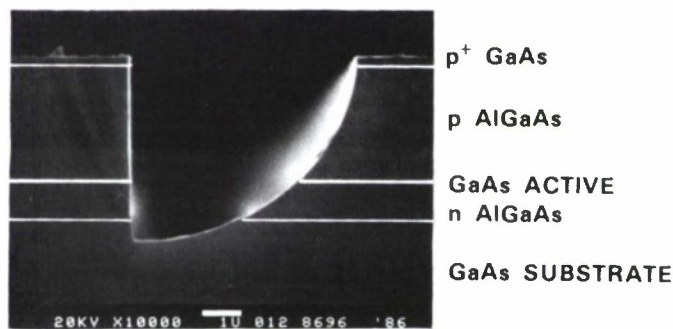
Figure 3-12. Scanning electron micrograph showing the cross section of a facet-deflector pair formed by Br:methanol etching.

REFERENCES

1. B-Y. Tsaur, R.W. Mountain, C.K. Chen, G.W. Turner, and J.C.C. Fan, IEEE Electron Device Lett. **EDL-5**, 238 (1984).

2. B-Y. Tsaur and H.K. Choi, IEEE Electron Device Lett. **EDL-7**, 324 (1986).

3. J.C.C. Fan, B-Y. Tsaur, and M.W. Geis, J. Cryst. Growth **63**, 453 (1983).

4. J.N. Walpole and Z.L. Liau, Appl. Phys. Lett. **48**, 1636 (1986).

5. T.H. Windhorn and W.D. Goodhue, Appl. Phys. Lett. **48**, 1675 (1986).

6. R.D. Burnham, D.R. Scifres, and W. Streifer, Electron. Lett. **17**, 714 (1981).

4. MICROELECTRONICS

4.1 POINT-CONTACT TRANSISTORS AND SCHOTTKY DIODES FORMED ON SYNTHETIC BORON-DOPED DIAMONDS

Point-contact transistors have been formed on the (100) surface of a synthetic diamond doped on the order of 10^{16} cm^{-3} with boron, as shown schematically in Figure 4-1(a). The collector and emitter contacts consist of tungsten probes, separated by a few tens of micrometers, that form Schottky diodes with the diamond. The base ohmic contact was formed either with tungsten probes or with a carbon film on the heavily doped (111) diamond surface. The properties of the resulting transistors varied considerably, with some of the better devices having current gains from 2 to 25 and power gains from 6 to 35. Figure 4-1(b) shows the collector current vs collector-base voltage for several emitter-base voltages.

Schottky diodes also were fabricated on diamond, as indicated in Figure 4-2(a), and exhibited stable I-V characteristics at temperatures in excess of 700°C. At temperatures at or exceeding 700°C, the diodes exhibited hysteresis upon forward bias, as shown in Figure 4-2(b), a behavior that we believe is related to trap states in the band gap. The Schottky characteristics degrade irreversibly above 800°C.

This is, to the best of our knowledge, the first report of devices formed in diamond that exhibit power gain in excess of unity. Further, this is the first report of a semiconductor diode operating in excess of 700°C. These results demonstrate the feasibility of forming practical devices in very high band gap semiconductors.

M.W. Geis   R.A. Murphy
D.D. Rathman   W.T. Lindley
D.J. Ehrlich

EMITTER   COLLECTOR

TUNGSTEN PROBES

P⁻

P⁺

DIAMOND SUBSTRATE

TUNGSTEN

BASE

OHMIC CONTACT

(a)

COLLECTOR CURRENT (mA)

≃3.5 V EMITTER-BASE VOLTAGE PER STEP

COLLECTOR-BASE VOLTAGE (V)

(b)
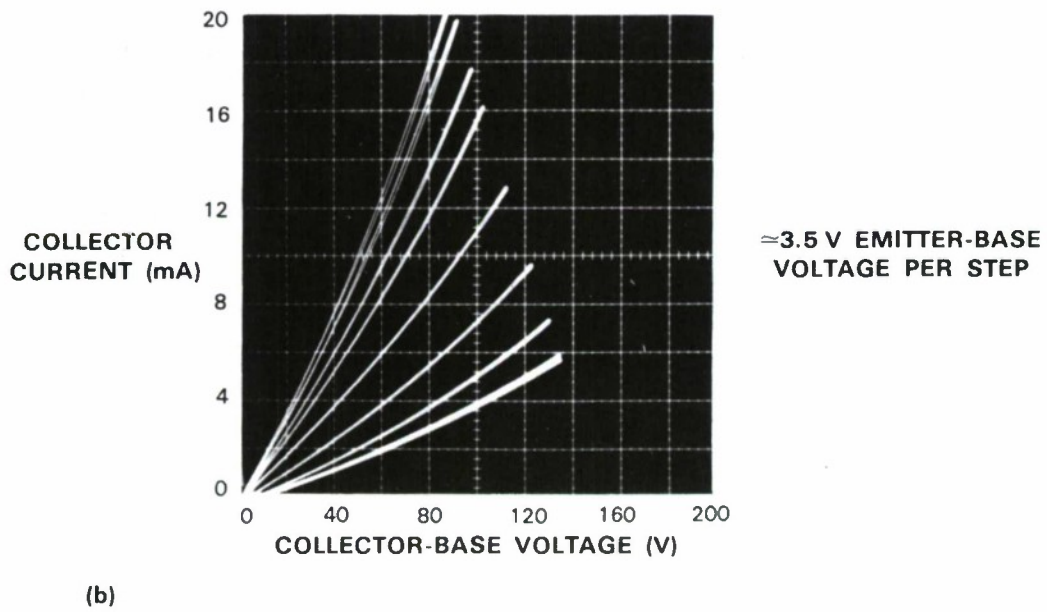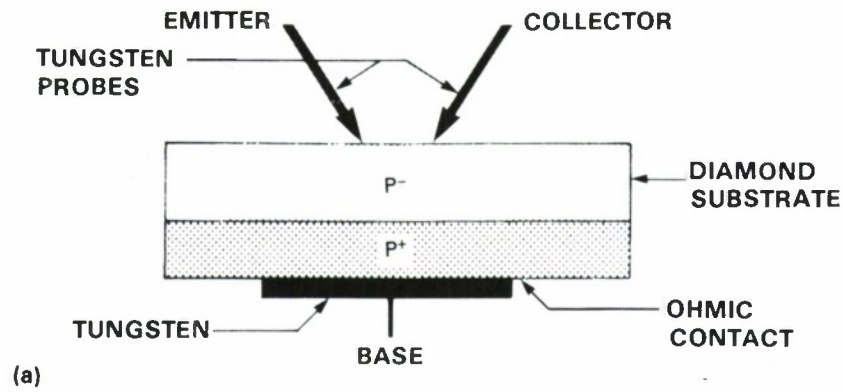
Figure 4-1. (a) *A schematic drawing of a point contact transistor formed on the (100) surface of a diamond.* (b) *The common base characteristics of the transistor.*
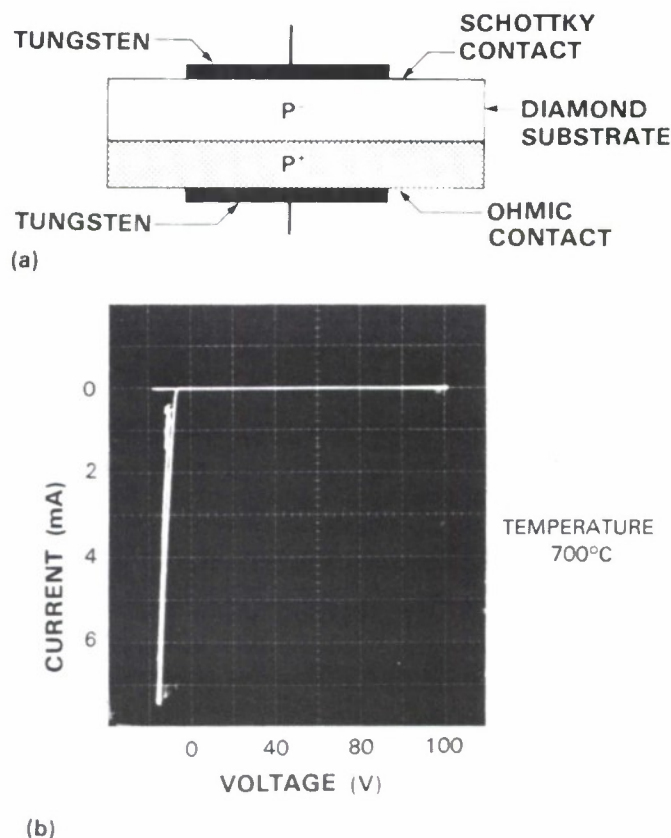
Figure 4-2. (a) A schematic drawing of a Schottky diode formed on the (100) surface of a diamond. The Schottky diode consisted of 30 nm of tungsten, 20 nm of titanium, and 100 nm of gold e-beam evaporated and patterned into 25-μm squares. (b) The voltage-current characteristics of the diode at 700° C. Note the hysteresis in the left quarter of the curve.

4.2 ANGULAR CHLORINE ION-BEAM-ASSISTED ETCHING OF GaAs AND AlGaAs

A variety of electronic and optical GaAs/AlGaAs-based devices require channels with sloping walls in GaAs and AlGaAs layers. We have used chlorine ion-beam-assisted etching (IBAE) to control wall slopes. In the IBAE process, an argon ion beam and a jet of chlorine gas are simultaneously incident on the sample. The etching is highly anisotropic, controlled by the argon ion beam. The wall slope is determined by the angle at which the sample is tilted with respect to the ion beam. Contours have been generated both by using fixed tilt angles and by computer-controlled dynamic tilting.

The basic chlorine IBAE process has been described by Geis et al.[1] To their apparatus has been added a cryopump, Meissner coil, second chlorine tube, load-lock, and tiltable sample holder. This system routinely reaches a background pressure of 1×10^{-7} Torr within fifteen minutes after a sample is transferred into the system.

37

A schematic of the etching geometry and computer-controlled sample stage used for angular etching is shown in Figure 4-3. Figure 4-4 shows SEM micrographs of etched walls in (100) GaAs with the edge alignment along the (011) cleavage plane. The first micrograph shows a sidewall etched at four different tilt angles for four different time intervals. The tilt-angle schedule was 30° for 20 min, 40° for 10 min, 50° for 5 min, and 60° for 2.5 min. The etched sidewall angles are identical to the tilt angles of the substrate with respect to the ion beam, and the etch rate is constant in the direction of the ion beam and independent of tilt angle. The second micrograph shows a curved sidewall obtained by computer-controlled etching using 800 discrete tilt angles. Etching was initiated with the ion beam 30° from the normal to the sample, and the angular motion of the sample holder was accelerated during the run. As the angle between the ion beam and the sample normal increases, the top edge of the mask shadows areas with more vertical sidewalls, so that virtually any concave shape can be generated. Convex sidewalls could be obtained by combining substrate tilting with computer-controlled variation in the argon ion beam current density. However, the motion required to generate convex shapes is more complicated because the entire sidewall is etching during the full run.

We have used the angular etching technique to produce surface-emitting diode lasers. The processing techniques used to prepare the wafers for etching have been described previously.[2] Figure 4-5 is a schematic of a surface-emitting laser and shows the relationship between the etched facet and 45° deflecting mirror. We plan to replace the 45° deflecting mirror with a curved mirror to add focusing capability and permit the fabrication of two-dimensional CW
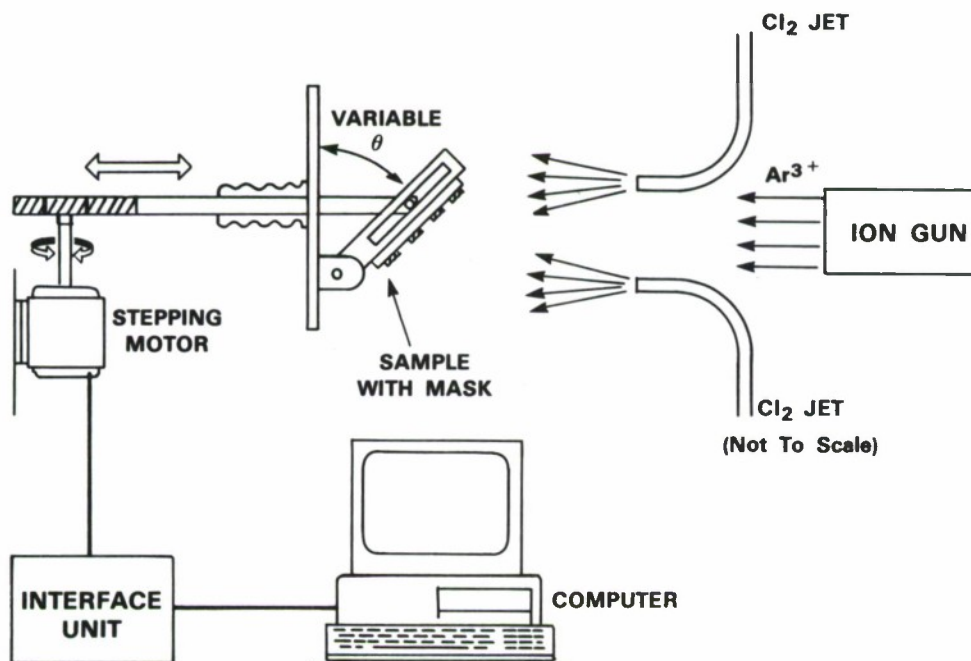
Figure 4-3. Schematic showing the etching geometry for the computer-controlled stage.

38
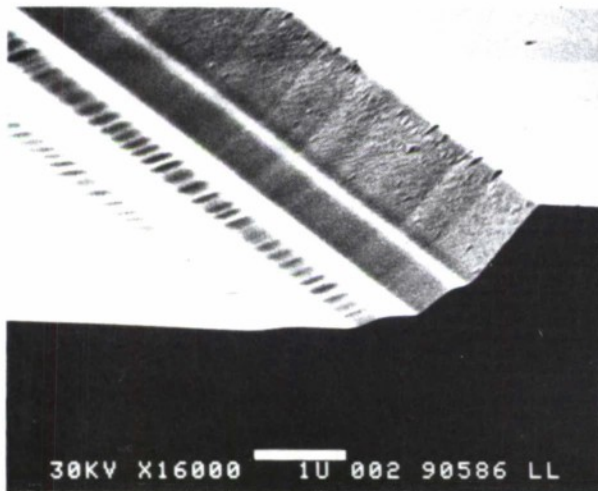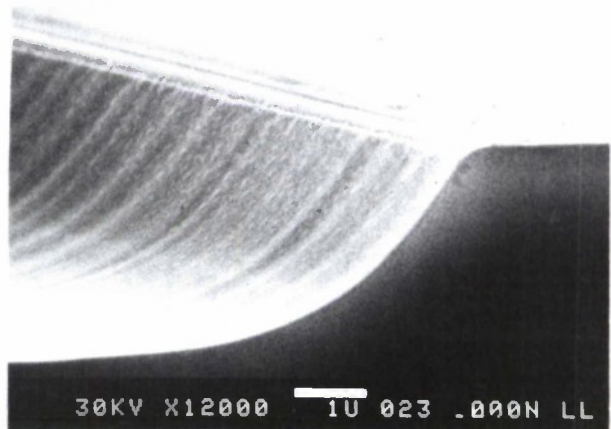
Figure 4-4.   SEM micrographs of etched sidewalls in GaAs. (a) Sidewall contour generated by four discrete angle runs at varying times. (b) Sidewall contour generated by computer-controlled continuous angle variation.

←—250 μm—→
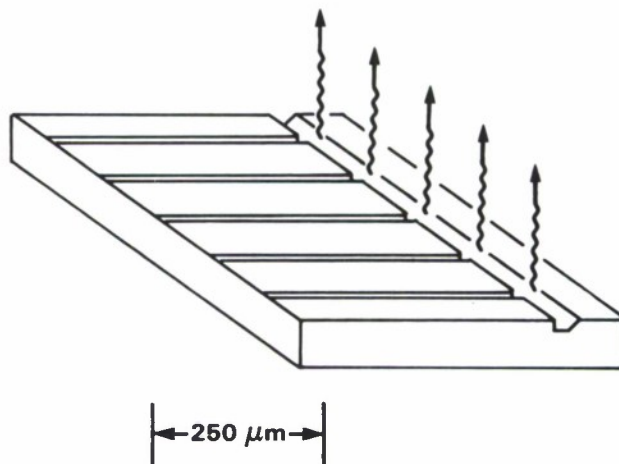
Figure 4-5.   Schematic of a surface-emitting laser device showing the relationship between the etched facet and deflecting mirror.

room-temperature arrays for high-power applications. Since the technique produces minimal surface damage,[1] we also are investigating its use in combination with molecular beam epitaxy overgrowth and as a method for etching relatively easily fabricated, 80-nm-wide quantum wires or boxes down to 10-20 nm for quantum confinement studies (Figure 4-6).
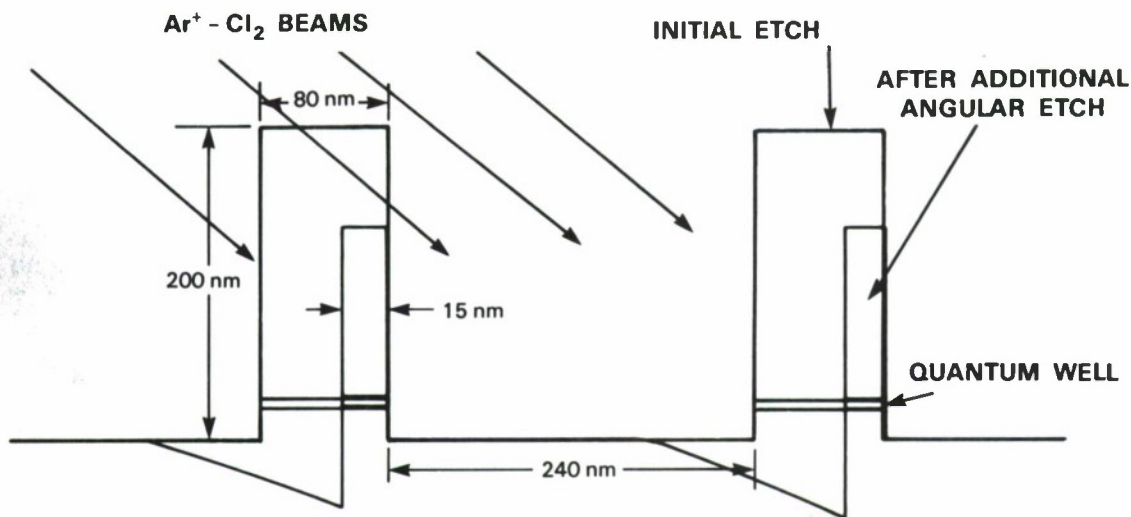
Figure 4-6. Schematic showing how quantum lines or boxes could be generated in a two-step etching process. After the initial etch, the masking layer is removed and a second angular etch is used to thin the columns.

In summary, chlorine IBAE has been used to etch channels in GaAs and AlGaAs, producing sidewalls tilted at the same angle as the substrate is tilted with respect to the ion beam. Both planar and curved sidewalls have been generated. Only minor orientation effects have been observed for the limited number of orientations investigated. The etching technique is potentially very useful for a variety of electronic and optical GaAs/AlGaAs devices.

<div align="right">

W.D. Goodhue   T.H. Windhorn
G.D. Johnson   S.W. Pang

</div>

4.3 CHARGE AMPLIFICATION IN A CHARGE-COUPLED DEVICE USING IMPACT IONIZATION

Charge-coupled device (CCD) image sensors have found widespread use in applications that require high quantum efficiency and low noise. Quantum efficiencies exceeding 50% already have been demonstrated in visible-band imagers; thus, further improvements in sensitivity must come mainly from reducing the device noise. This is particularly true at high output clock rates, since the noise, which arises principally from the output FET charge detection circuit, scales as the square root of the clock rate. This suggests that one approach to overcoming this limitation is the use of predetection charge amplification. We have studied a method of charge amplification

using impact ionization in the high-field region between adjacent CCD gates, and we report here measurements of avalanche-induced gain and noise on small charge packets.[3]

Avalanche multiplication in a surface channel CCD has been reported by Madan et al.,[4] who gave measurements of gain as a function of clock voltages but no data on noise. Since the usefulness of this process depends to a great extent on its noise properties, we measured both gain and noise. Special attention was given to minimizing competing noise sources in the device so that avalanche-induced noise could be measured accurately. Devices with an n-type buried channel were used to avoid transfer efficiency noise associated with surface-state trapping. Dark current noise was eliminated by cooling the device to –80°C. The output charge detection circuit on these CCDs is designed for low noise performance, and in combination with low noise off-chip signal processing, we routinely obtained noise levels equivalent to nine electrons rms at a 500-kHz output clock rate.

Figure 4-7 depicts a portion of a CCD used for the avalanche gain measurements. The procedure uses three independently biased gates (G1, 2, 3) and begins with G1 set to a 'high'
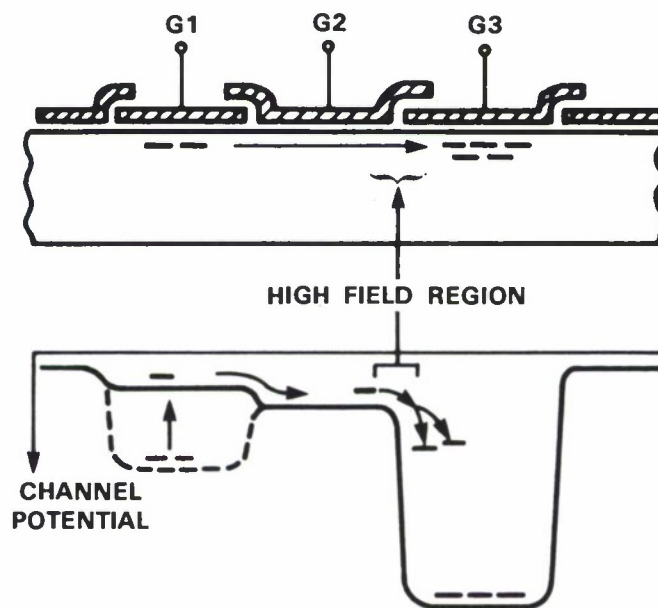
Figure 4-7. *Cross-sectional view of the CCD gate structure used in the avalanche gain measurements. Also depicted is the channel potential during charge transfer from G1 to G3 and the impact ionization that occurs in the high-field region between G2 and G3.*

state of approximately 10-12 V and the remaining gates biased to a 'low' state of –2 to 0 V. A light source above the device is pulsed on to provide a controlled source of photoelectrons, and these carriers are collected by G1. After the light is turned off, gate G3 is raised to a voltage sufficiently high that the electric field in the channel between G2 and G3 can cause impact

41

ionization. Gate G1 then is lowered toward −2 V, causing the photoelectrons to transfer through the high-field region and into the G3 well. Because the high field region is so narrow (less than 1 μm), the probability of an ionization event is low. Therefore, we transfer the charge from G3 back to G1 and repeat the sequence several times in order to obtain large gain.

When the light source is off and the dark current is unmeasurably low, a spurious charge is generated when ΔV, the voltage difference between G3 and G2, exceeds approximately 20 V. This charge has been noted previously,[4] but its origin is uncertain at present. The quantity of charge generated is several hundred electrons at the highest gain levels used, and the amplitude and noise associated with this signal have been removed from the data that follow. Figure 4-8 shows the final versus initial packet size after 200 transfers for various values of ΔV. The gain is essentially unity up to ΔV = 20 V, but rises rapidly as the voltage is increased above this level. At 26 V, the gain is 2.50 and the gain per transfer inferred from this is 1.0046.
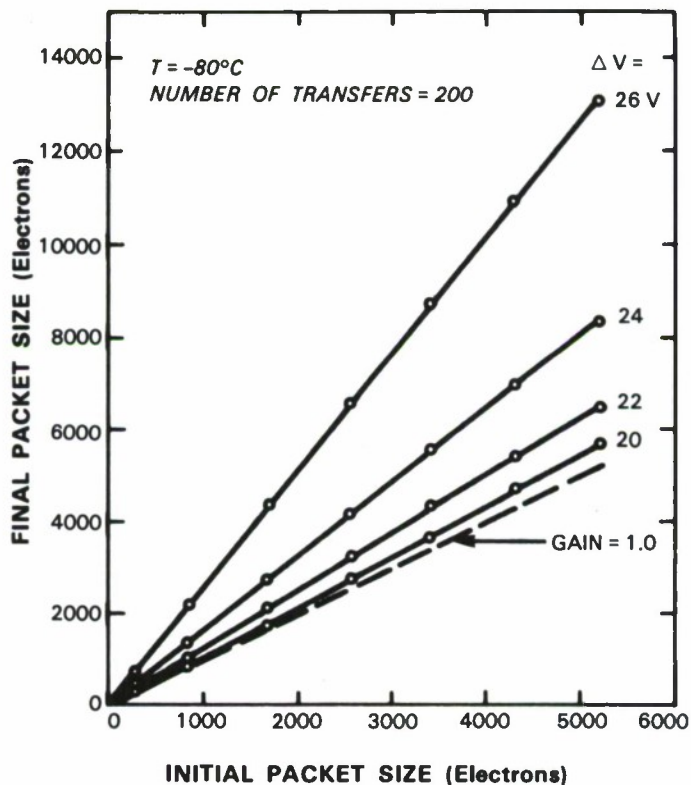
Figure 4-8. Measured data showing final vs initial packet size for different values of ΔV, the potential difference between G3 and G2.

A general theory of carrier multiplication noise for one-carrier processes has been given by Van Vliet and Rucker.[5] For the conditions of this experiment, a simple derivation of their result can be obtained by noting that, since the gain per transfer, m, is close to unity, we can assume at

42

most one ionization per primary carrier transit through the high field region. The contribution of the holes is neglected because their ionization coefficient is much less than that of the electrons in silicon and because they are removed from the charge packet after each transfer. Each carrier transit then can be regarded as a Bernoulli trial with probability $p = m - 1$ of an ionization event. The variance σ_1^2 of the number of carriers for one transfer is thus $\sigma_1^2 = m^2\sigma_0^2 + \bar{n}(0)(m-1)(2-m)$ where $\bar{n}(0)$ and σ_0^2 are the mean and variance of the initial electron packet. After N identical stages of gain, the variance is

$$\sigma_N^2 = M^2\sigma_0^2 + \bar{n}(0) \, (M^{2-1/N} - M^{1-1/N}) \, (2 - M^{1/N}) \tag{4-1}$$

where $M = m^N$ is the total gain. Since $M^{1/N} = m \simeq 1$, we can simplify Equation (4-1) to

$$\sigma_N^2 = M^2\sigma_0^2 + \bar{n}(0)M(M - 1) \quad . \tag{4-2}$$

Measured values for the noise versus gain are given in Figure 4-9 for an initial charge packet of 1530 electrons. The bias voltage $\triangle V$ was varied from 22 to 27 V, although additional
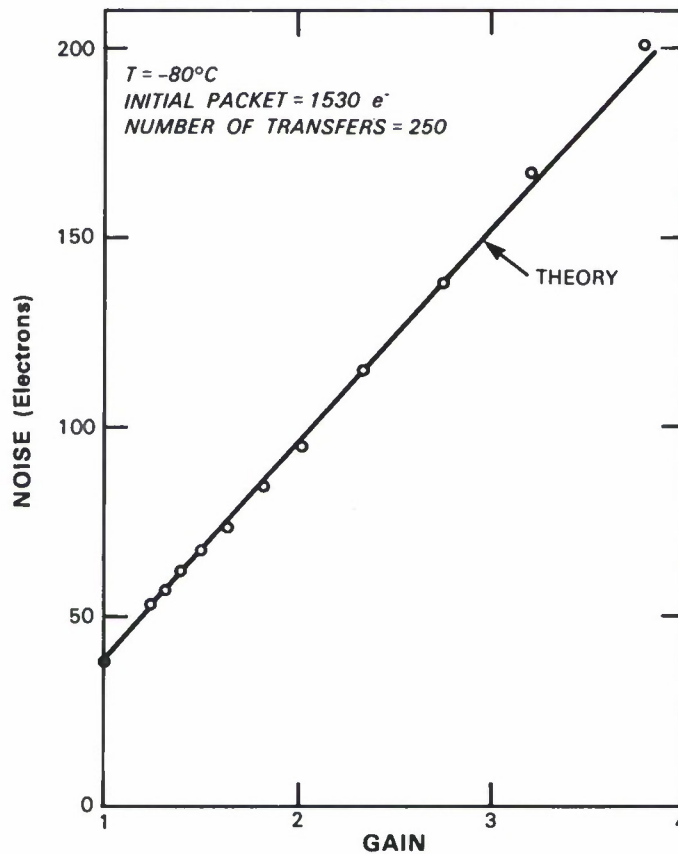
Figure 4-9. Experimental and theoretical values of noise vs gain for a charge packet initially having 1530 electrons.

measurements with fixed ΔV and varying numbers of transfers gave virtually identical results. Shown for comparison is the prediction of Equation (4-2) with $\sigma_0{}^2 = 1530$ electrons; the agreement with the experimental results is good.

Because of the noise associated with the spurious charge generation, we were unable to investigate the regime of greatest interest, namely, the gain and noise associated with much smaller charge packets near or below the output circuit noise level. We currently are attempting to understand the origin of this spurious charge.

<div style="text-align: right">

S.A. Gajar
B.E. Burke

</div>

4.4 MASKED ION BEAM LITHOGRAPHY FOR SUBMICROMETER-GATE-LENGTH TRANSISTORS

GaAs MESFETs with 0.3-μm gate length have been fabricated using masked ion beam lithography (MIBL) to define the self-aligned submicrometer gates and optical lithography to define areas for contact pads and device isolation. The fabricated devices have a transconductance of 150 mS/mm.

MIBL, employing stencil masks with transmission holes in SiN_x membranes,[6] was used for the first mask level, which consisted of submicrometer gates self-aligned to the source and drain patterns. Films of 0.5-μm-thick SiO_2 and 1-μm-thick SiN_x were deposited on Si substrates for stencil mask fabrication. Electron-beam lithography and dry etching techniques were used to define the submicrometer gate openings as well as the source and drain openings in the SiN_x films. The gate lengths were varied from 0.1 to 0.3 μm, the width was 23 μm, and the source to drain spacing was 3 μm. Then the Si substrates and oxide layers were etched away, leaving free standing SiN_x membranes for the stencil masks.

GaAs samples, with n-type epitaxial layers grown on semi-insulating substrates, were used for MESFET fabrication. The detailed fabrication sequence is illustrated in Figure 4-10. Figure 4-11 shows MESFET patterns defined by exposing 500-nm PMMA through a stencil mask using MIBL. It is found that the variation in exposure dose and development time does not have significant effects on the PMMA linewidth control.[7] With PMMA as the etching mask, self-aligned source, drain, and gate patterns are defined in the SiO_2 by reactive-ion etching in CF_4 at 250 V. The high aspect ratio structure, formed in the combined PMMA and SiO_2 layers used to define the submicrometer gate, allows ohmic metals to be deposited only in the source and drain regions and not in the gate region via shadow evaporation. The rest of the patterning for contact pads, device isolation, and T-gate overlay was done by optical lithography. Figure 4-12 shows a SEM micrograph of a T-gate structure made using a 1-μm overlay mask on top of a 0.15-μm oxide opening.

Figure 4-13 shows typical current-voltage characteristics of 0.3-μm-gate-length GaAs MESFETs fabricated using the MIBL technique described above. The transconductance is 150 mS/mm at zero gate bias and the pinch-off voltage is 2 V. The devices also show good

MIBL EXPOSURE

DEFINED SOURCE,
DRAIN AND GATE

OHMIC METAL

ANGLE EVAPORATION

METAL LIFTOFF

T-GATE LIFTOFF
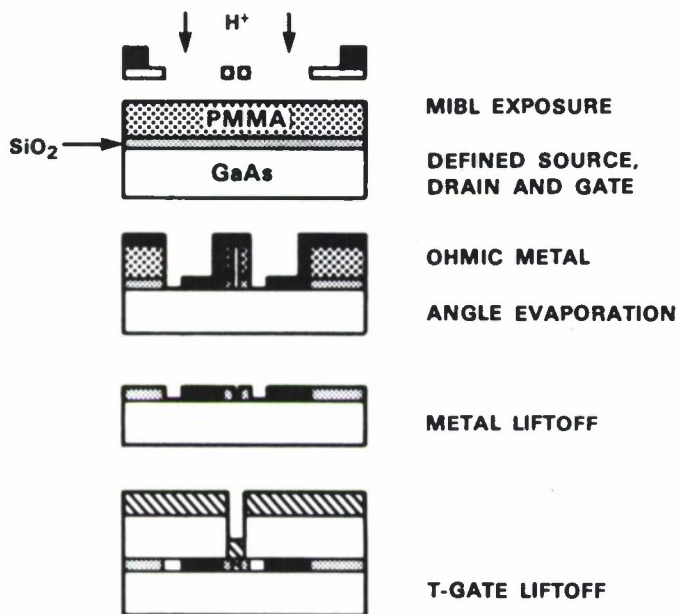
Figure 4-10. Fabrication procedure for self-aligned MESFETs.

Figure 4-11. Self-aligned MESFET patterns defined by exposing 500-nm PMMA through stencil mask using MIBL. A 50-keV proton beam and a total dose of 2×10^{13} ions/cm^2 was used.

45

|←——1 μm——→|
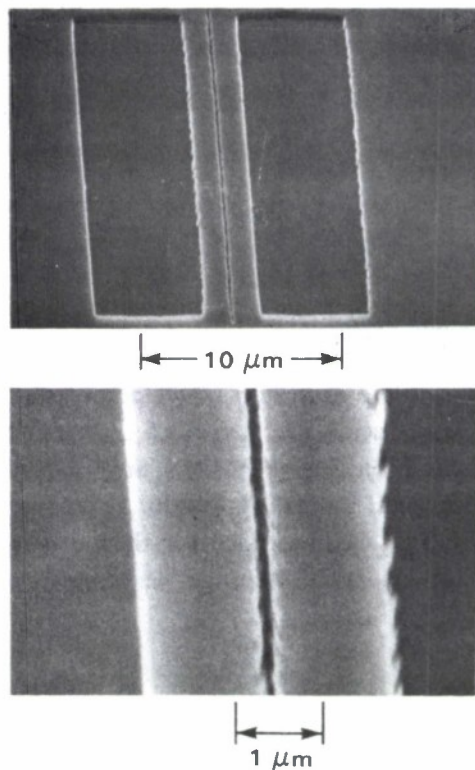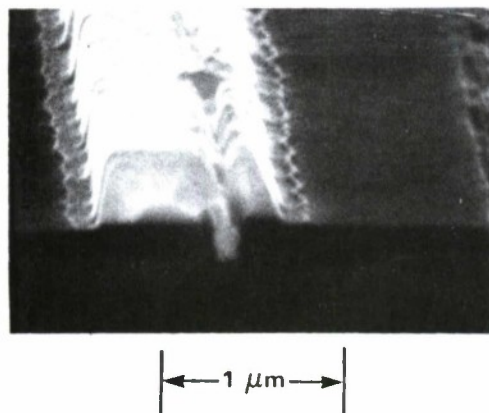
Figure 4-12. *T-gate structure that consists of a 1-μm gate overlaid on a 0.15-μm gate length.*

g_m = 150 mS/mm
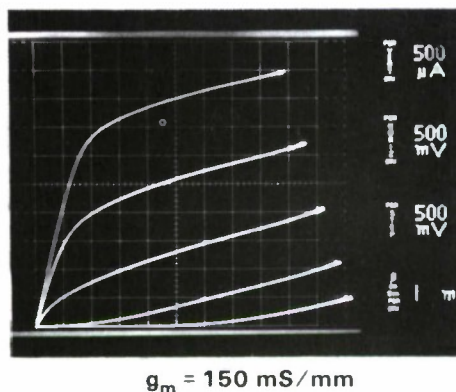
Figure 4-13. *I-V characteristics of the fabricated MESFET with 0.3-μm gate length.*

Schottky diode characteristics with a reverse breakdown voltage of 10 V. A maximum frequency of oscillation of 20 GHz is obtained from the RF measurement of the devices.

The radiation effect of protons on GaAs was studied, and it was found that proton penetration into the GaAs substrates should be minimized to avoid ion-induced damage. With the combination of PMMA and SiO_2 layers, the residual damage in GaAs can be recovered by thermal annealing at 450°C for 5 s or by wet etching to remove 50 nm of the top surface. Since a SiO_2 layer is used for the self-aligned submicrometer gate definition and the gate is recessed by wet chemical etching, the radiation effect in the GaAs substrate is expected to be controllable.

S.W. Pang   J.P. Donnelly
T.M. Lyszczarz   J.N. Randall
C.L. Chen

46

REFERENCES

1. M.W. Geis, G.A. Lincoln, N. Efremow, and W.J. Piacentini, J. Vac. Sci. Technol. **19,** 1390 (1981).

2. T.H. Windhorn and W.D. Goodhue, Appl. Phys. Lett. **48,** 1675 (1986).

3. S.A. Gajar, M.S. Thesis, Massachusetts Institute of Technology, August 1986.

4. S.K. Madan, B. Bhaumik, and J.M. Vasi, IEEE Trans. Electron Devices **ED-30,** 694 (1983).

5. K.M. Van Vliet and L.M. Rucker, IEEE Trans. Electron Devices **ED-30,** 746 (1979).

6. J.N. Randall, D.C. Flanders, N.P. Economou, J.P. Donnelly, and E.I. Bromley, J. Vac. Sci. Technol. **B3,** 58 (1985).

7. J.N. Randall, E.I. Bromley, and N.P. Economou, J. Vac. Sci. Technol. **B4,** 10 (1986).

5. ANALOG DEVICE TECHNOLOGY

5.1 A HIGH-SPEED TWO-DIMENSIONAL CCD GAUSSIAN IMAGE CONVOLVER

We report here the demonstration of the first imager working at standard television rates that can convolve a scene with an electronically adjustable Gaussian kernel function. The significance of Gaussian image convolution lies in its application in the difference-of-Gaussians (DOG) edge-detection algorithm developed at the MIT Artificial Intelligence Laboratory.[1] This algorithm is able to discriminate objects based on their spatial extent by suppressing detail that is finer than the width of the Gaussian kernel function. The algorithm has not found widespread practical application because of the computational load imposed on image-processing systems by convolutions with kernels of up to 25-by-25 pixels applied to image fields with 10^5 to 10^6 pixels.

In a previous contribution,[2] we described in detail the new technique we use for producing the Gaussian convolution of an image stored in a charge-coupled device (CCD) imager and presented experimental results obtained with a one-dimensional CCD. The technique can be summarized very briefly as follows: Under the application of suitable clocking waveforms, charge packets in the CCD are caused to mix with neighboring packets sequentially in each direction. This causes the charge in each pixel to spread out in a diffusive manner described very accurately by Gaussian convolution. The mixing cycles are repeated until the desired degree of spreading has been achieved. By using physical rather than computational principles and by applying them to all or large groups of pixels simultaneously, very high-speed processing is achieved.

There are two general ways to use the technique to carry out two-dimensional Gaussian convolution. A CCD that can perform charge transfers in two dimensions can carry out the convolution on an entire image completely in parallel. In this case, a Gaussian convolution equivalent to digital convolution with a 25-by-25-pixel kernel matrix can be performed on an image of arbitrarily large size in less than 100 μs. Alternatively, one can generate a two-dimensional Gaussian convolution using a sequence of one-dimensional convolutions. That is the method we have demonstrated.

A Thomson-CSF type TH-7861 frame-transfer, 288-by-384 pixel, four-phase CCD imager was used in our experiments. Its structure is illustrated schematically in Figure 5-1. The image is formed in a section of the chip called the imaging zone, which comprises an array of 384 vertical linear imagers each containing 288 active pixels. Charges are collected for a period of time and then transferred rapidly to a frame memory zone comprising a similar array of linear CCD registers. While the next image is being collected in the imaging zone, the charges in the memory zone are transferred one TV line at a time into a horizontal serial output shift register with a length of 384 active pixels. Each line is read out at high speed so that the entire image in the memory zone has been clocked out by the time the imaging zone has collected a new image.

For our experiments, we constructed a special timing generator that could operate the device with the additional mixing cycles needed to generate the Gaussian convolution of the stored image. To conform to National Technical Standards Committee (NTSC) RS-170 video timing
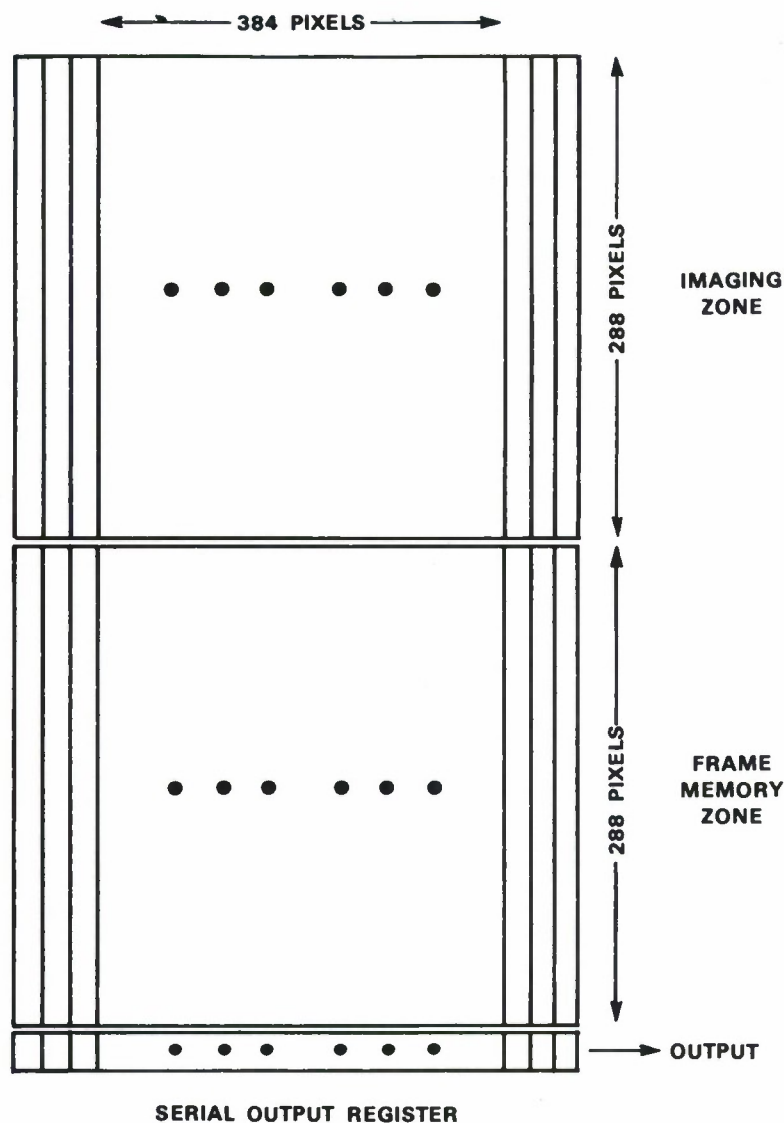
Figure 5-1. *Basic organization of CCD imaging chip used to make two-dimensional Gaussian convolution.*

standards, we used only 256 of the 288 lines. The timing is illustrated in Figure 5-2. Images are collected for a period of 1/60 s. During the vertical blanking interval of about 380 μs, the image is transferred to the memory zone using 290 standard clocking cycles (288 active pixels plus 2 inactive pixels). Then during the remaining 32 μs of vertical blanking time, all of the registers in the memory zone are subjected to a number of Gaussian mixing cycles that can be varied from 0 to 39. This effects the vertical Gaussian convolution.

Next, each of 256 lines is read out sequentially as follows. First, one pixel from each of the vertical linear CCDs in the memory zone is transferred into the horizontal serial register. This
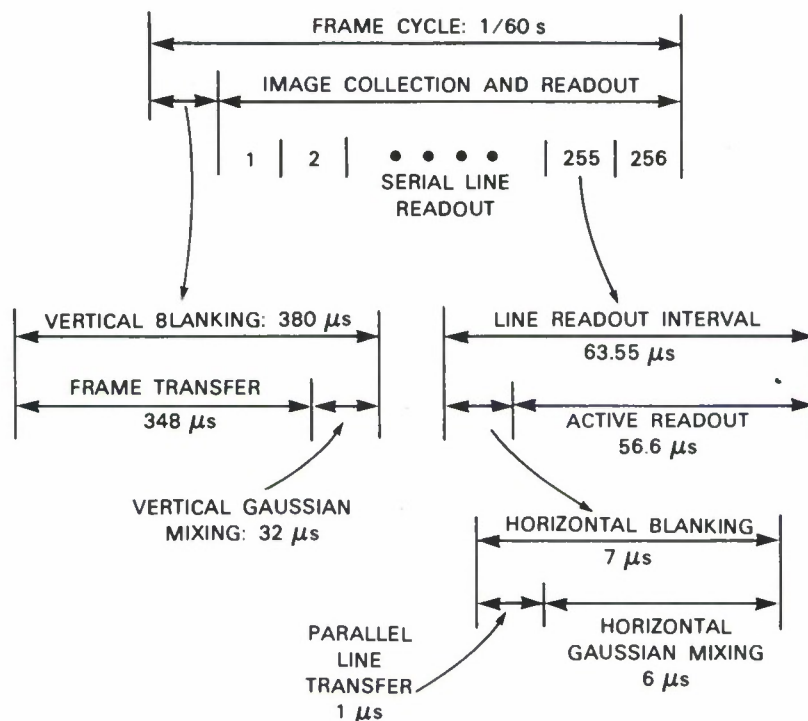
Figure 5-2. Timing diagram showing how Gaussian mixing is carried out within the NTSC RS-170 timing constraints.

register has a total of 405 cells, 384 for the image and 21 additional for black-level reference and other special purposes. Before the register is transferred to the CCD output as in a conventional imager, it is subjected to the same number of Gaussian mixing cycles as the vertical registers were during the frame transfer time. A period of 63.55 μs is allocated for the readout of each line. With a clock frequency of 7.16 MHz, twice the color subcarrier frequency, the 405 readout clock cycles take 56.6 μs, leaving 7 μs of horizontal blanking time during which the parallel transfer of the line and the Gaussian mixing are performed. The former takes about 1 μs, leaving 6 μs for Gaussian convolution. At the same clock frequency, this allows up to about 40 mixing cycles.

The output from the CCD imager was fed to a digital frame-capture board in a computer, where the images were stored, displayed, and analyzed. Figure 5-3(a) shows a normal, unblurred image made using no Gaussian mixing cycles. Figures 5-3(b) and 5-3(c) show images read out using, respectively, 16 and 32 Gaussian mixing cycles in each direction. Finally, Figure 5-3(d) shows the results of subtracting the two Gaussian-convolved images and displaying (as white) only those pixels in which the difference is very close to zero. The edges of the larger objects are apparent; objects with fine detail reveal only their outer boundaries.
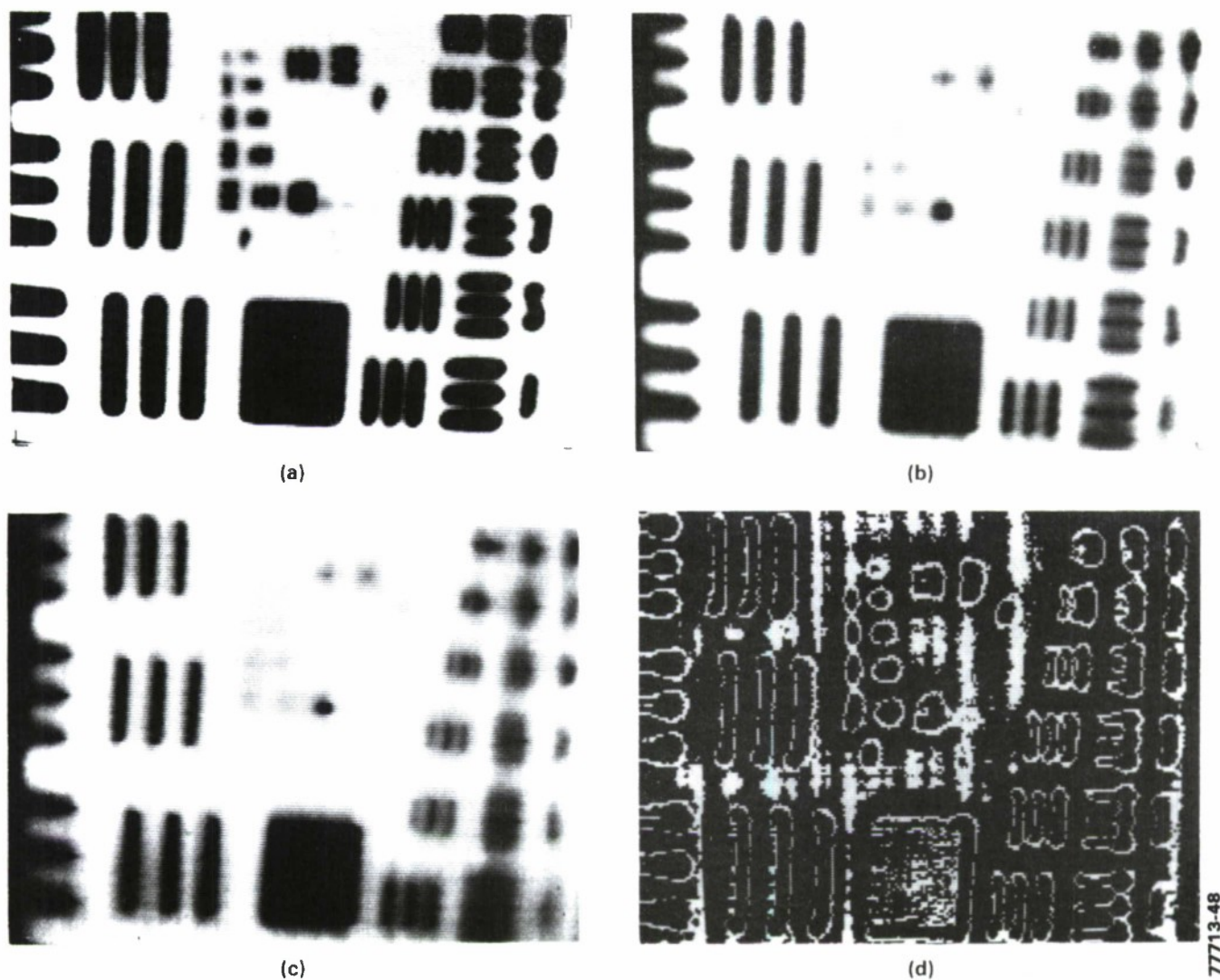
Figure 5-3. *(a) Unblurred image, (b) image after 16 Gaussian mixing cycles in each direction, (c) image after 32 Gaussian mixing cycles, and (d) example of DOG output using images (b) and (c).*

We have demonstrated that, with no more than modified control circuitry, a CCD imager of conventional design can perform electronically controllable Gaussian convolution. Consequently, this powerful image-processing function can be made available to a system with virtually no penalty in cost, size, or power. In the future, integrated circuits incorporating this technology along with other image-processing functions — such as image memory, differencing, thresholding, and histogram analysis — will bring image-processing functions down to the chip level.

J. P. Sage
A. L. Lattes

52

5.2 ADAPTIVE AND MATCHED FILTERING WITH A SAW/FET PROGRAMMABLE TRANSVERSAL FILTER

The surface-acoustic-wave/field-effect-transistor (SAW/FET) programmable transversal filter has matured recently to the point where the 350 taps now exhibit an on/off ratio of 30 dB. This improvement over the previously reported 20-dB on/off ratio[3] is shown in Figure 5-4 and was made possible by an increased range of programmable tap capacitance values. Together with a 100-MHz programmable bandwidth and a 1.5-μs-long impulse response, these specifications enable the device to be used in a wide variety of systems applications.

An important attribute of the SAW/FET device is that one may program its impulse response at rates compatible with digital signal processing systems (typically less than 20 MHz), yet process (filter) signals in real time whose bandwidths are up to 100 MHz. We have demonstrated such operation by programming the device as a matched filter for both 31-chip and 63-chip m-sequences. The results of the correlation of the slowly programmed (1 MHz) impulse response and the wideband RF input are shown in Figures 5-5 and 5-6. Figure 5-5(a) shows the 31-chip m-sequence programmed into the device via the multiplexed FET array (top trace), along with the wideband m-sequence input to the edge-bonded transducer (middle trace), and the resulting correlation output (bottom trace). Notice that the output consists of multiple correlation spikes, consistent with the repetitive m-sequence RF input. Figure 5-5(b) shows a time-expanded view of one of these correlation spikes. The sidelobe level is down by 27 dB from the correlation peak, within 2 dB of the theoretical value. Figure 5-6 demonstrates matched filtering of a 63-chip sequence in the same manner.

We have configured the SAW/FET for adaptive filtering by adding an adaptive control loop based on the least-mean-squares (LMS) algorithm.[4,5] We have demonstrated cancellation of CW interference using this automatic, interactive process of successive approximation where the required tap-weight updates are calculated in a digital computer, loaded into a buffer memory, and then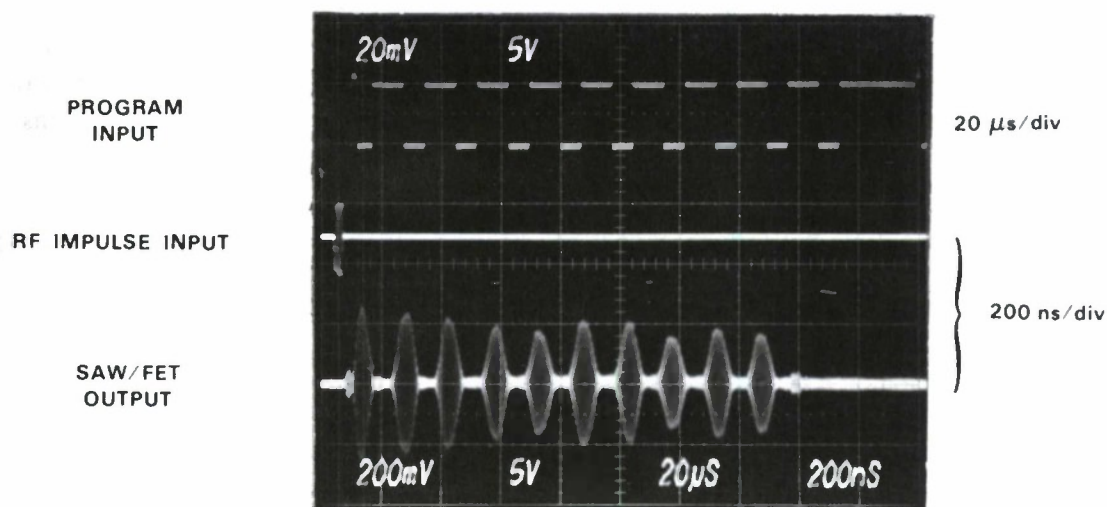 serially reprogrammed into the SAW/FET programmable transversal filter (PTF) through a digital-to-analog (D/A) converter (Figure 5-7). The use of the SAW/FET allows operation on wideband signals, while the system adaptation time is determined by the computer-based implementation.

In order to illustrate the operation of the LMS algorithm, we configured the SAW/FET-based adaptive filter to implement a CW interference canceler. The first experiment demonstrated single-tone cancellation in an application where one is presented with an interference signal of unknown frequency. During the adaptation time, the host system would turn off its own transmission. In the demonstration of this adaptation, the single-frequency interference is fed to both the x and d inputs (Figure 5-7). Over the course of the adaptation time, the filter sets a narrow passband at the input frequency and adjusts the 350 stored tap weights so that the SAW/FET output y has the same phase and amplitude as the signal d. This effects a cancellation in the difference amplifier and thus minimizes the signal e. After the system adapts, one would then resume broadband communications, with the CW interference signal eliminated.

PROGRAM
INPUT

RF IMPULSE INPUT

SAW/FET
OUTPUT

20mV   5V

20 μs/div

200 ns/div

200mV   5V   20μS   200nS

(a)

SAW/FET OUTPUT
WITH 20-dB
ADDITIONAL GAIN

20mV   200nS

(b)

77713-49
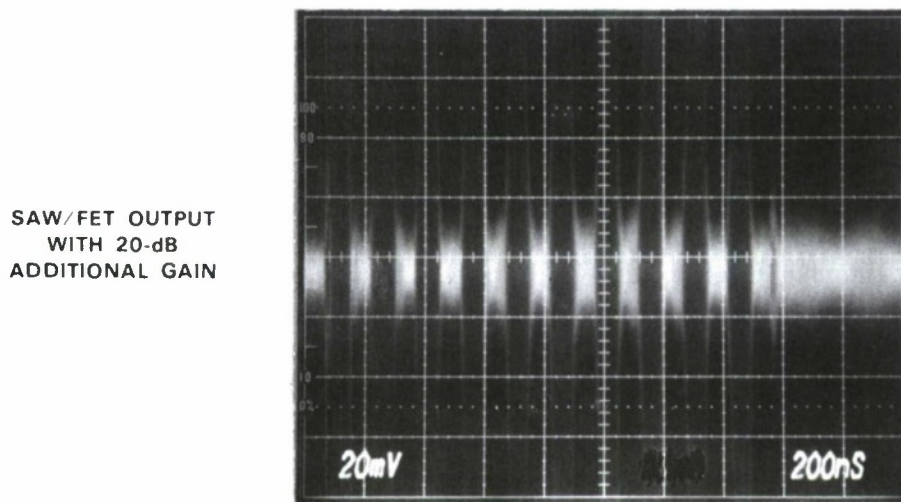
Figure 5-4.   Demonstration of 30-dB programmable on/off ratio of SAW/FET. (a) Top trace: low-speed programming of the device, turning alternate groups of taps fully on and off. Middle trace: RF input, a 175-MHz-carrier impulse. Bottom trace: device output. (b) Device output with 20-dB additional gain, demonstrating the on/off ratio. Most of the signal from the 'off' finger groups is thermal noise, as evidenced by its continuation past the 1.5-μs impulse response duration.

54

Figure 5-5. (a) *Top trace: 31-chip m-sequence programmed at low speed into SAW/FET. Middle trace: wideband RF input of repetitive m-sequence. Bottom trace: SAW/FET output.* (b) *Top trace: expanded view of correlation peak. Bottom trace: correlation sidelobes amplified by 20 dB.*

55

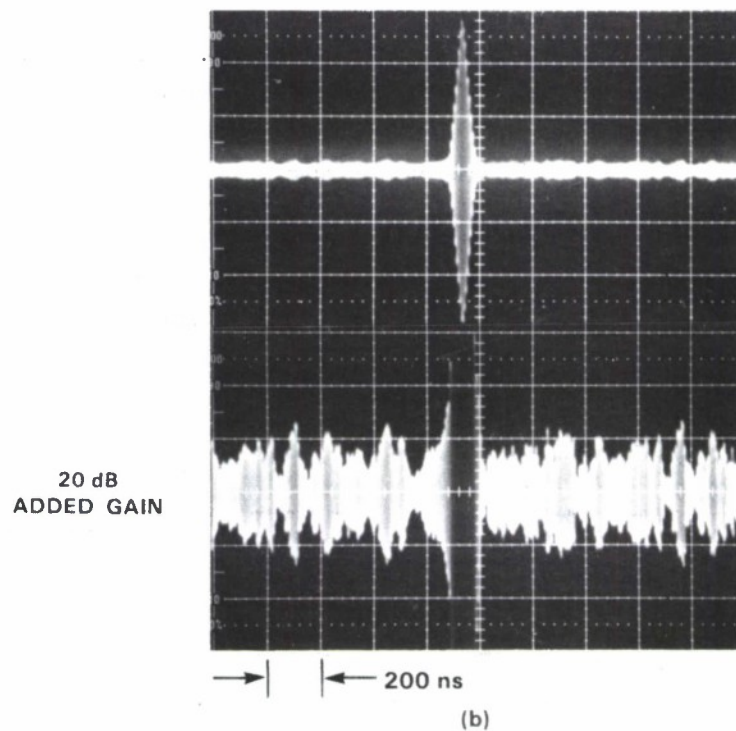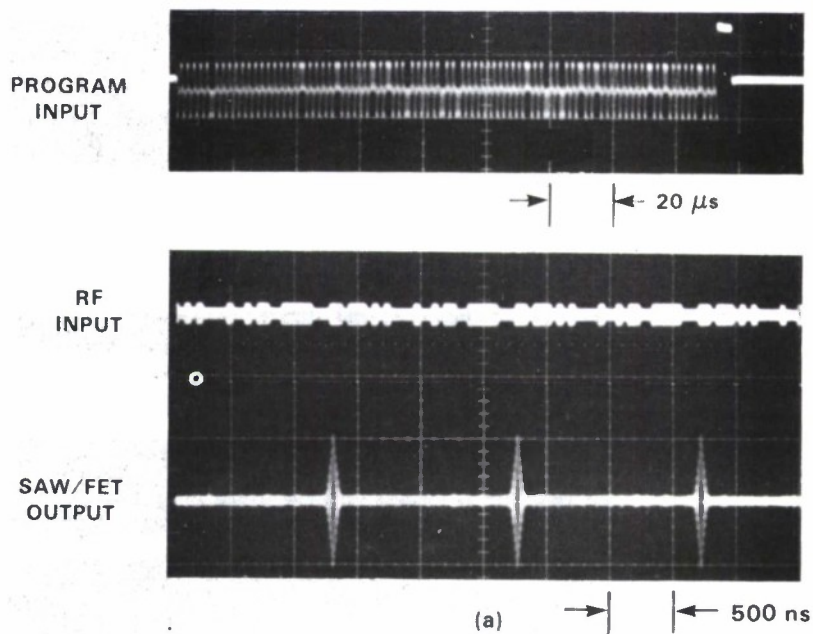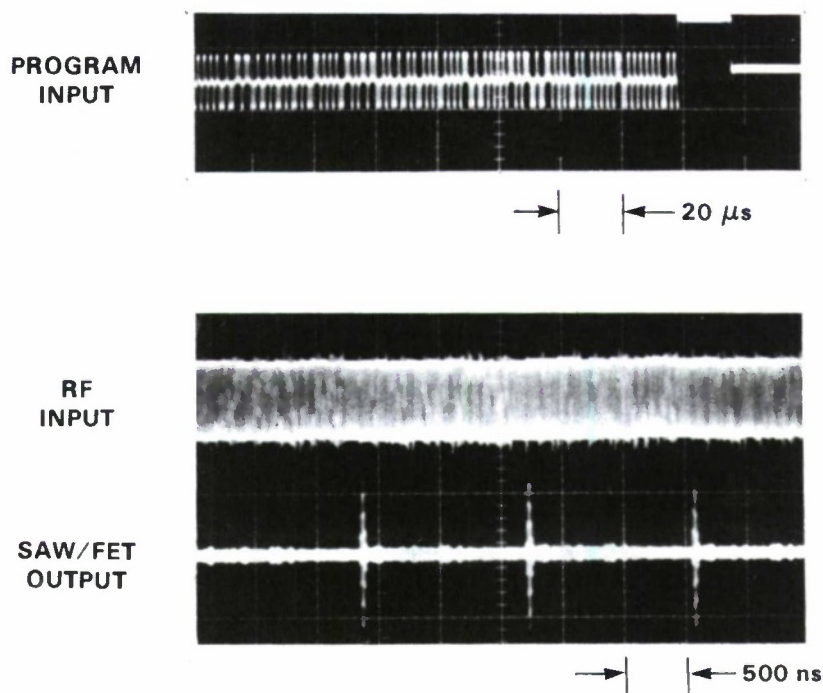*Figure 5-6. Top trace: 63-chip m-sequence programmed at low speed into SAW/FET. Middle trace: wideband RF input of repetitive m-sequence. Bottom trace: SAW/FET output.*
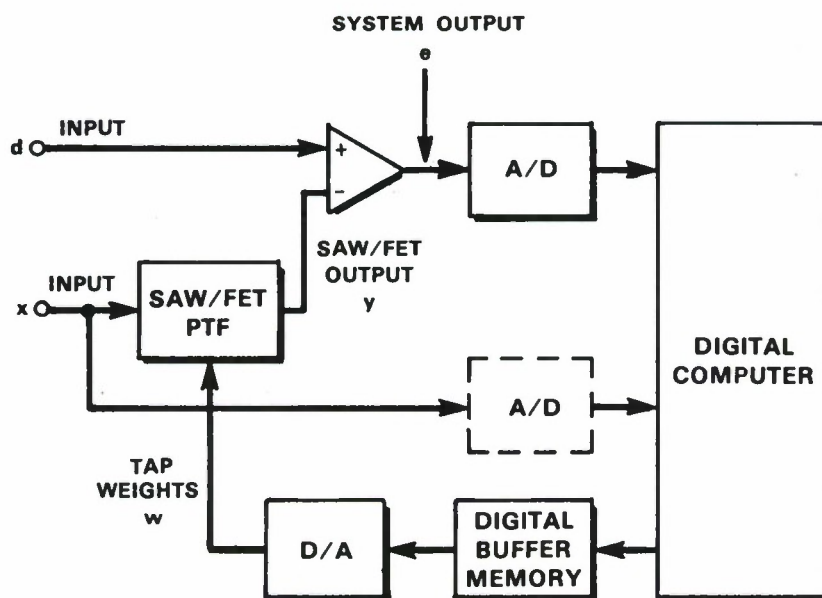
Figure 5-7. Block diagram showing SAW/FET-based adaptive filter system.

56

The cancellation was measured consistently in the range 22-25 dB for various values of the relative phase between the d and x inputs and with a ±5-dB range of relative power level for the signal input at d. The resulting passband notch width was 700 kHz, corresponding to the 1.5-μs interaction region of the SAW/FET device.

The adaptive filter performance is demonstrated in Figure 5-8 for the case of two combined sinusoids at 140 and 180 MHz fed to the input d while the 180-MHz tone, which was to be
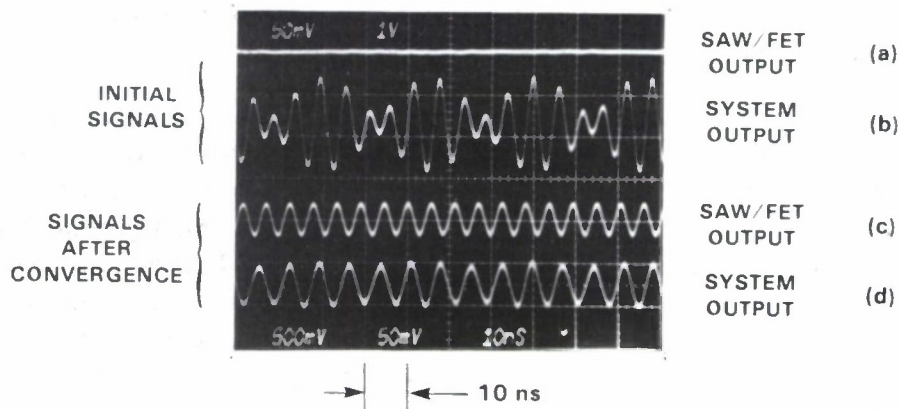
Figure 5-8. Outputs from adaptive filter when canceling 180-MHz component from an input signal comprising 180- and 140-MHz tones: (a) initial SAW/FET output, (b) initial system output, (c) converged SAW/FET output showing amplitude- and phase-matched 180-MHz tone, (d) converged system output with 180-MHz component canceled.

suppressed, was fed to the x input. An application of this mode of operation might be found in an instance where the frequency of the interfering signal is known, but not its amplitude and/or phase. In this case, the system is allowed to adapt even during information transmission. Figure 5-8 shows in the upper two traces the initial signal conditions. The SAW/FET initially has no output signal (because all tap weights are zero) and the signal e (which represents the system output) comprises the two sinusoids. The lower two traces show these same measurements after convergence in 44 iterations. The output of the SAW/FET now passes the 180 MHz tone with the proper amplitude and phase, so that the resulting signal seen at the output of the difference amplifier contains only the 140-MHz signal; the 180-MHz tone has been adaptively suppressed by 24 dB. With a 2-MHz SAW/FET programming clock rate, the update cycle for each iteration took typically 30 s. Most of this time was devoted to loading the 350 weight values from the computer over the IEEE-488 data bus into the buffer memory. Custom adaptive control circuits could reduce the adaptation time to less than 1 ms.

57

Although the above demonstration showed single-tone interference suppression, the SAW/FET device is also capable of performing multiple-tone suppression over a 100-MHz bandwidth. The SAW/FET programmable transversal filter is the widest-bandwidth device showing large analog tap-programmability with an architecture enabling its simple interface to digital systems.

J. B. Green   P. M. Grant
D. E. Oates   D. L. Smythe

5.3 COUPLING OF PHASE AND AMPLITUDE ADJUSTMENTS IN LASER-COMPENSATED RACs

Earlier,[6] we applied laser direct-writing techniques to trim amplitude and phase characteristics of a reflective-array compressor (RAC) on YZ-LiNbO$_3$. We had employed a basic averaging algorithm on the measured frequency-domain data to define the required spatial compensation patterns used for phase and amplitude correction. This algorithm presumed that spatial phase corrections affected only the phase response in the frequency domain and that spatial amplitude corrections affected only the amplitude response in the frequency domain. It further presumed that corrections in space are mapped into the frequency response by a simple linear mapping between space and frequency based on the device chirp slope and acoustic propagation velocity. This approach was adequate for demonstration of the *in situ* compensation technique but not for actual RAC production.

In fact, a spatial correction in amplitude or phase affects both the amplitude and phase response in the frequency domain over a range of frequencies wider than indicated by the linear mapping. In order to obtain an accurate spatial-domain compensation pattern, one must deconvolve the effect of a complex grating kernel function from the measured response in the frequency-domain data. Several RAC models of varying complexity exist from which the required kernel function can be determined. Notably, the continuous weak-reflection model developed at Hughes[7] is amenable to efficient computational analysis and, to date, has been extremely useful in describing ideal RAC response. This result can be modified to include the effects of amplitude and phase distortions as[8]

$$
\Gamma(\Delta\omega) = \exp\left[-i\ \frac{c(\Delta\omega)^2}{4\pi v^2}\right]\ \int_{-\infty}^{\infty}\ \text{Rect}\left(\frac{z}{L}\right)\ \gamma(z)\left(\frac{\rho(z)}{\lambda(z)}\right)^2 \times
$$

$$
\times\ \left\{\frac{1}{W}\ \int_{-\infty}^{\infty}\ \text{Rect}\left(\frac{x}{W}\right)\ \exp\left[i\ \frac{\pi}{c}\left(\frac{c\Delta\omega}{2\pi v}-z-x\right)^2\right]dx\right\}^2\ dz \qquad , \qquad (5\text{-}1)
$$

where $\Gamma(\Delta\omega)$ is the RAC transfer function and $\gamma(z)$ represents the amplitude and phase distortion lumped into an effective perturbation in the strip between the two gratings (Figure 5-9). Also, Rect (x) = 1 for $-0.5 < x < 0.5$ and 0 otherwise, $\Delta\omega = \omega - \omega_c$ where ω_c is the device center frequency, v is the acoustic propagation velocity, $c = Tv^2/2B$ where B is the device bandwidth and T is its dispersion, $\rho(z)$ is the groove reflectivity, $\lambda(z)$ is the synchronous wavelength, L is the grating length, and W is the grating width.

58
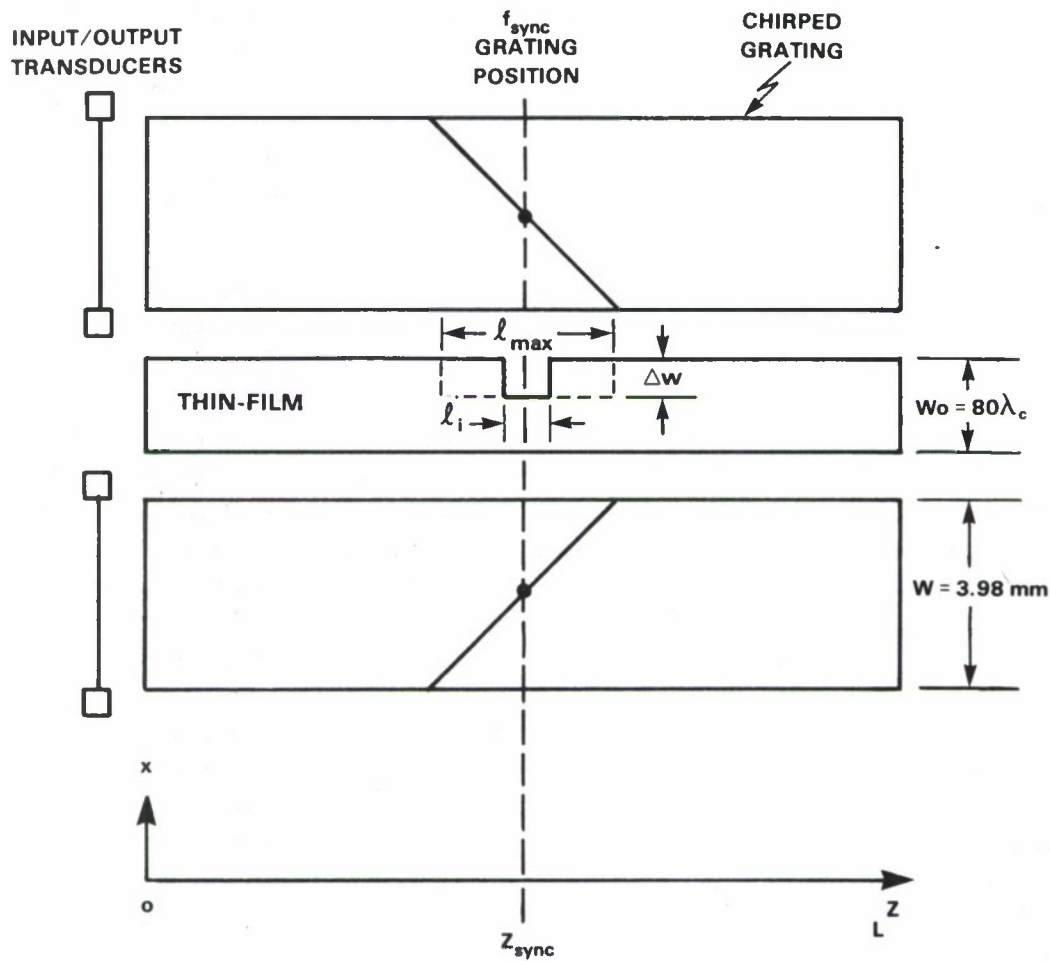
Figure 5-9. Schematic diagram of RAC with compensation film. Step-like notches of varying lengths ℓ_i centered on z_{sync} and constant width Δw are laser-etched sequentially into thin films of Cr-Cr$_2$O$_3$ or Mo to provide controlled amplitude or phase distortion, respectively. The grating width W was designed to be $N_{eff}\lambda$ for this device.

In the simplest application of Equation (5–1), it was shown[8] that an independent application of either a small phase or an amplitude correction resulted in a response with strong coupling of the amplitude and phase characteristics. Recently, we performed a sequence of experiments to quantify this result and thus determine the applicability of the weak-reflection model as the basis for a compensation algorithm for device correction.

Several down-chirp RACs with midband frequency of 106 MHz were configured with either a featureless 400-$\mathring{A}$-thick Mo film or 250-$\mathring{A}$-thick Cr-Cr$_2$O$_3$ cermet film between the gratings for phase or amplitude compensation, respectively. Each was approximately 80λ wide along the full length of the grating, where λ_c is the wavelength of device center frequency. Subsequently, within each strip, a sequence of notches of increasing length was laser-etched, centered on a value of z

corresponding to a specific frequency. This is illustrated schematically in Figure 5-9. The Mo films were etched in Cl_2 as described previously.[6] The cermet films were laser-modified in O_2; previously,[6] an indirect process in which an electrically shorting Mo film was stripped from the cermet in Cl_2 had been employed. Amplitude and phase response were measured after definition of each notch. The length of the laser-etched notch varied from 0.05 N_{eff} to 0.8 N_{eff}, where N_{eff} is the effective number of adjacent grooves that contribute to the response at any single frequency. In these devices $N_{eff} = 120$ and corresponds to 12% of the entire device.

Calculated RAC transfer characteristics and experimental results representative of a notch sequence laser-etched into phase- and amplitude-compensation films are summarized in Figures 5-10 and 5-11, respectively. After analysis of measured device data, a sliding window average on the data has removed a periodically varying ripple. The rapidly varying residual ripple is attributed to the limits of analyzer measurement accuracies in conjunction with the environmental conditions of the experimental setup. Both shape and magnitude of the coupled amplitude and phase response are in very good agreement with computations. For notch widths less than N_{eff}, which can be shown to approximate the convolution kernel width, the frequency interval over which the device response is appreciably affected is insensitive to the spatial extent of the applied perturbation. Experimentally, this behavior is most evident in the amplitude responses. An artifact of the phase-fitting routine complicates the straightforward presentation of this characteristic in the phase response of the device to an induced phase perturbation, as shown in Figure 5-10. The effect of a second notch centered on 106.2 MHz is evident at the high-frequency end of the measured results in this figure. For these narrow notches, peak deviations in the coupled response increase proportionally with increasing notch size. Quantitative agreement between peak measurements and calculations is generally better than 5%. The failure of the calculations to exhibit the measured asymmetry results from the omission in the weak-reflection model of wave depletion, multiple reflections, and stored-energy effects at the groove edges, each of which are thought to contribute to the observed asymmetry.

Other experiments are planned in order to further characterize the cermet film selected for amplitude compensation. Additionally, several RACs will be fully compensated using a deconvolution of Equation (5-1) to extract $\gamma(z)$.

<div align="right">

V. S. Dolat
J. H. C. Sedlacek

</div>

Figure 5-10. (a) Measured, and (b) calculated device response to a sequence of small step-like phase distortions introduced by localized laser-etching of Mo film. Notch lengths $\ell_{1i}/N_{eff}\,\lambda$ (i = 1, . . . , 4) are increased by factors of 2 from 0.05 to 0.4. Here, $\Delta w = 400\ \mu m$ and corresponds to $-32°$ of phase change at $f_{sync} = 104.6\ MHz$. Synchronous frequency range spanned by each notch and by N_{eff} is shown.
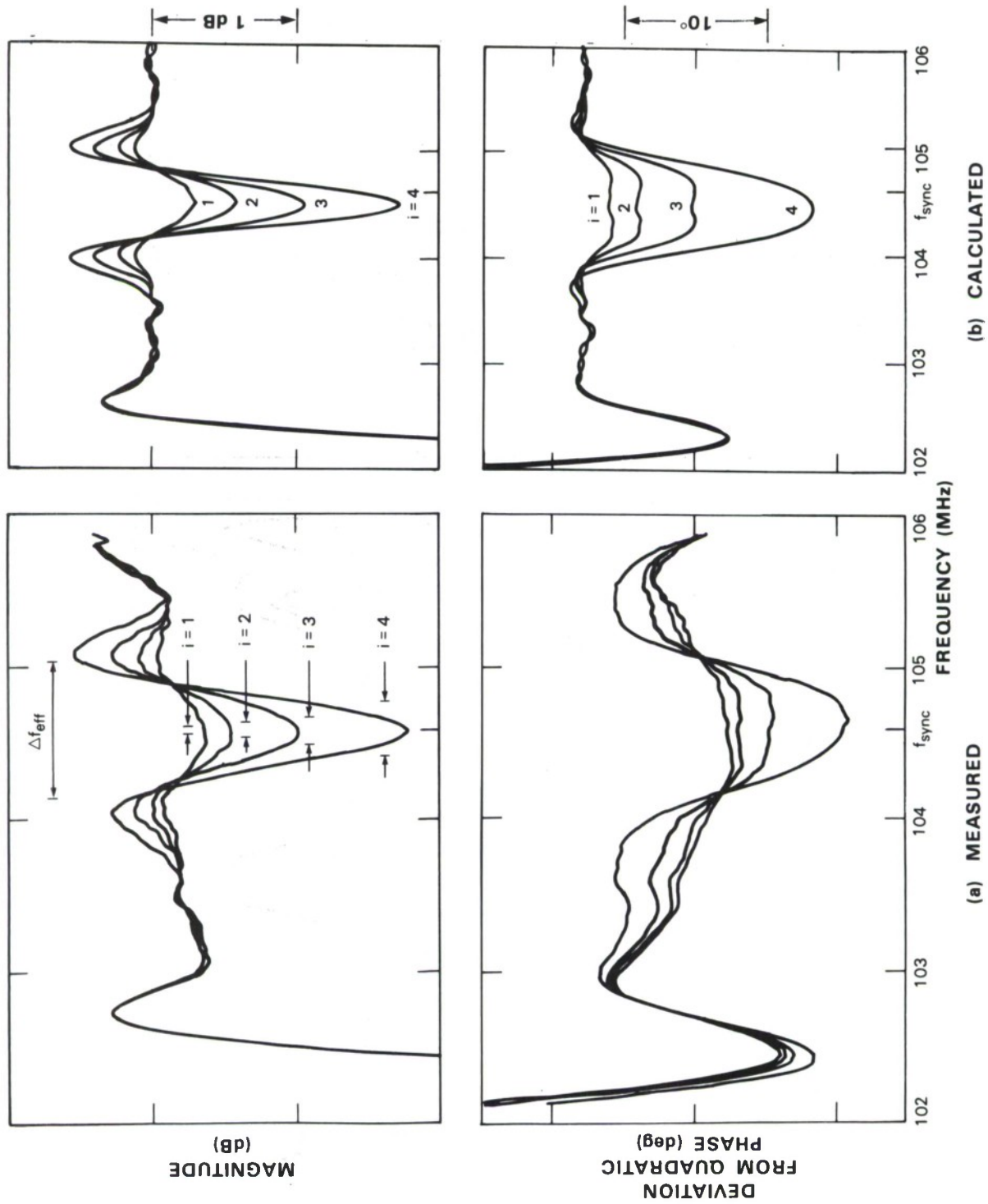
61
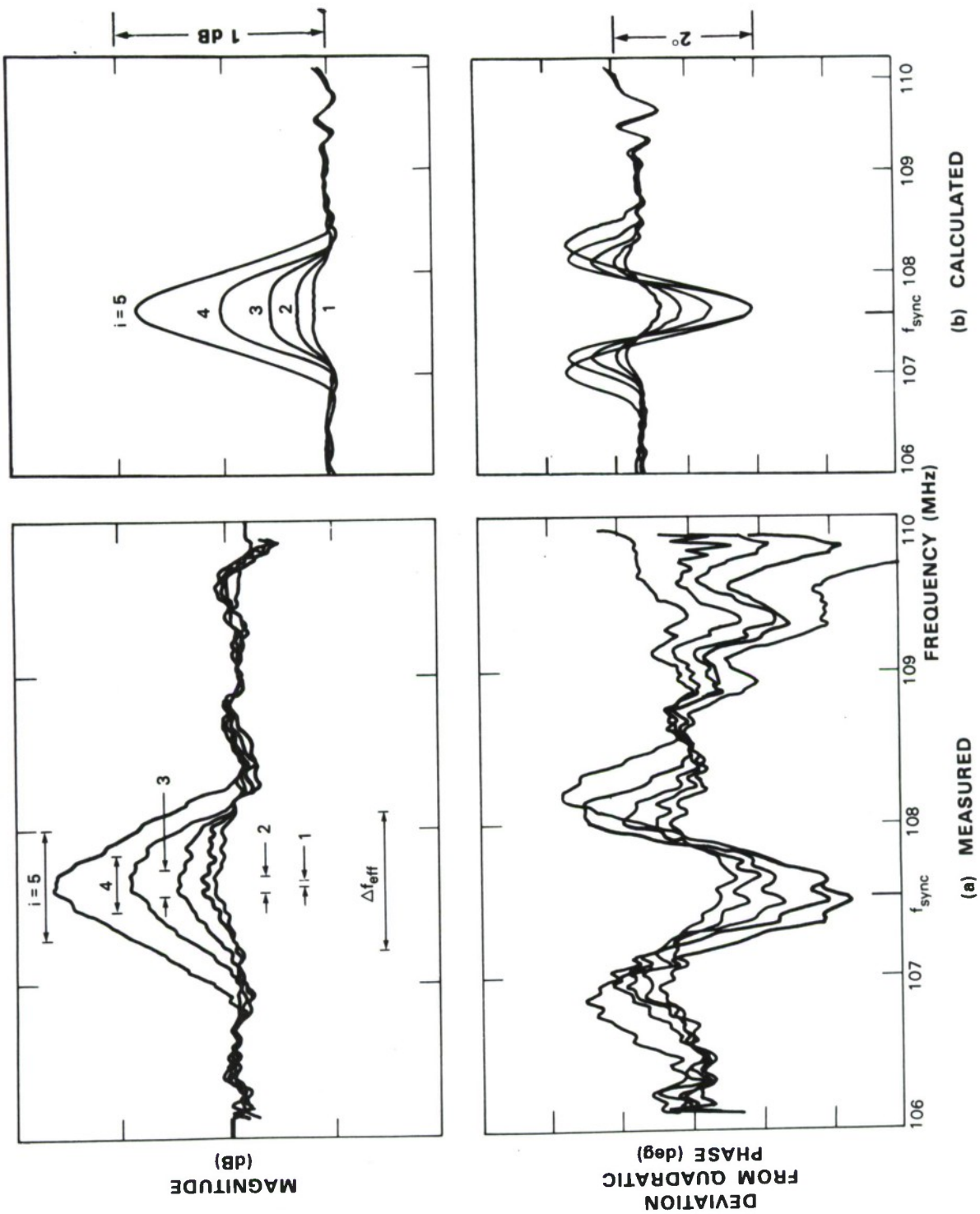
Figure 5-11. (a) Measured, and (b) calculated device response to a sequence of small step-like amplitude distortions introduced by local modification of Cr-Cr$_2$O$_3$ cermet film. Notch lengths $\ell_i/N_{eff}\lambda$ ($i = 1, \ldots, 5$) are increased by factors of 2 from 0.05 to 0.8. Here, $\Delta w = 800$ μm corresponds to ≈ 1-dB amplitude change at f_{sync} = 107.6 MHz. The synchronous frequency range spanned by each notch and by N_{eff} is shown.

77713-56

REFERENCES

1. D. Marr and E. Hildreth, Proc. R. Soc. London **B207**, 187 (1980).

2. Solid State Research Report, Lincoln Laboratory, MIT (1983:4),
   DTIC AD-A142991/9

3. D. E. Oates, D. L. Smythe, and J. B. Green, *1985 Ultrasonics Symposium Proceedings* (IEEE, New York, 1985), p. 124.

4. C. F. N. Cowan and P. M. Grant, *Adaptive Filters* (Prentice-Hall, New York, 1985).

5. D. E. Oates, J. B. Green, and P. M. Grant, Electron. Lett. **22**, 998 (1986).

6. Solid State Research Report, Lincoln Laboratory, MIT (1985:1),
   DTIC AD-A160922 p. 51.

7. H. M. Gerard, O. W. Otto, and R. D. Weglein, "Wideband Dispersive Surface Wave Filters," Report ECOM-73-0110-F, Hughes Aircraft Company, Ground Systems Group (December 1974), Appendix A.

8. T. A. Martin *1976 Ultrasonics Symposium Proceedings* (IEEE, New York, 1976), p. 411.

REPORT DOCUMENTATION PAGE		READ INSTRUCTIONS BEFORE COMPLETING FORM
1. REPORT NUMBER ESD-TR-86-135	**2. GOVT ACCESSION NO.**	**3. RECIPIENT'S CATALOG NUMBER**
4. TITLE *(and Subtitle)* Solid State Research		**5. TYPE OF REPORT & PERIOD COVERED** Quarterly Technical Report 1 August — 31 October 1986
		6. PERFORMING ORG. REPORT NUMBER 1986:4
7. AUTHOR(s) Alan L. McWhorter		**8. CONTRACT OR GRANT NUMBER(s)** F19628-85-C-0002
9. PERFORMING ORGANIZATION NAME AND ADDRESS Lincoln Laboratory, MIT P.O. Box 73 Lexington, MA 02173-0073		**10. PROGRAM ELEMENT, PROJECT, TASK AREA & WORK UNIT NUMBERS** Program Element No. 63250F Project No. 649L
11. CONTROLLING OFFICE NAME AND ADDRESS Air Force Systems Command, USAF Andrews AFB Washington, DC 20334		**12. REPORT DATE** 15 November 1986
		13. NUMBER OF PAGES 92
14. MONITORING AGENCY NAME & ADDRESS *(if different from Controlling Office)* Electronic Systems Division Hanscom AFB, MA 01731		**15. SECURITY CLASS.** *(of this Report)* Unclassified
		15a. DECLASSIFICATION DOWNGRADING SCHEDULE

16. DISTRIBUTION STATEMENT *(of this Report)*

Approved for public release; distribution unlimited.

17. DISTRIBUTION STATEMENT *(of the abstract entered in Block 20, if different from Report)*

18. SUPPLEMENTARY NOTES

None

19. KEY WORDS *(Continue on reverse side if necessary and identify by block number)*

solid state devices	lasers	surface acoustic wave devices
quantum electronics	laser arrays	quantum-well effects
materials research	signal processing	silicon-on-insulator devices
microelectronics	charge-coupled devices	radiation hardening
analog device technology		

20. ABSTRACT *(Continue on reverse side if necessary and identify by block number)*

This report covers in detail the solid state research work of the Solid State Division at Lincoln Laboratory for the period 1 August through 31 October 1986. The topics covered are Solid State Device Research, Quantum Electronics, Materials Research, Microelectronics, and Analog Device Technology. Funding is provided primarily by the Air Force, with additional support provided by the Army, DARPA, Navy, SDIO, NASA, and DOE.

DD FORM **1473** EDITION OF 1 NOV 65 IS OBSOLETE
1 Jan 73